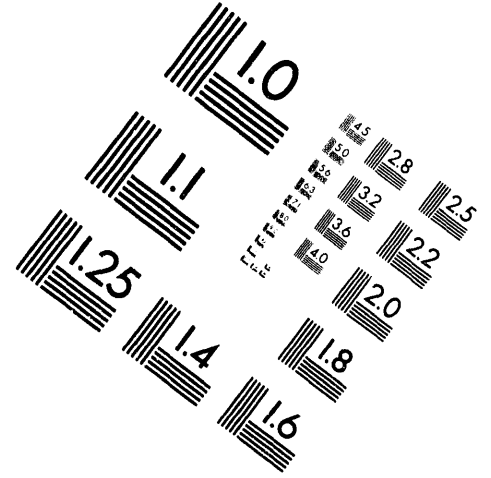
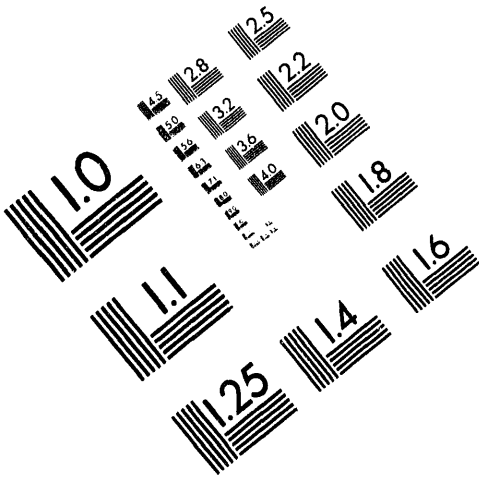




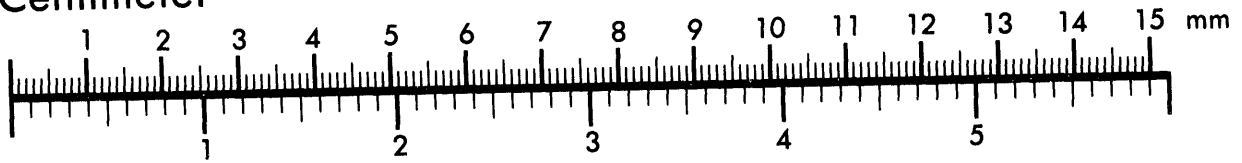
AIM

Association for Information and Image Management

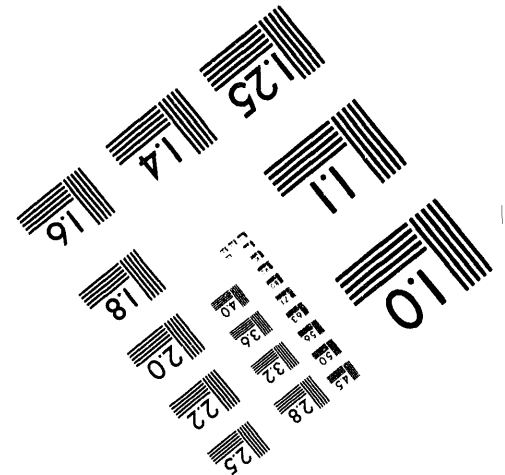
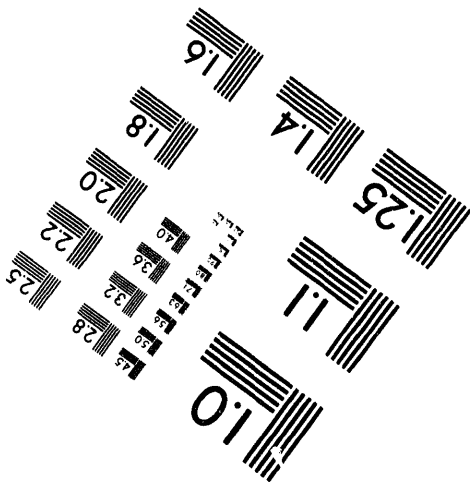
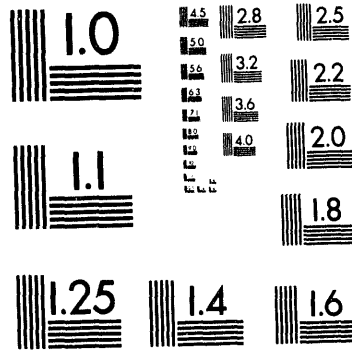
1100 Wayne Avenue, Suite 1100
Silver Spring, Maryland 20910
301/587-8202



Centimeter



Inches



MANUFACTURED TO AIM STANDARDS
BY APPLIED IMAGE, INC.

1 of 1

2)

Conf-940216--5

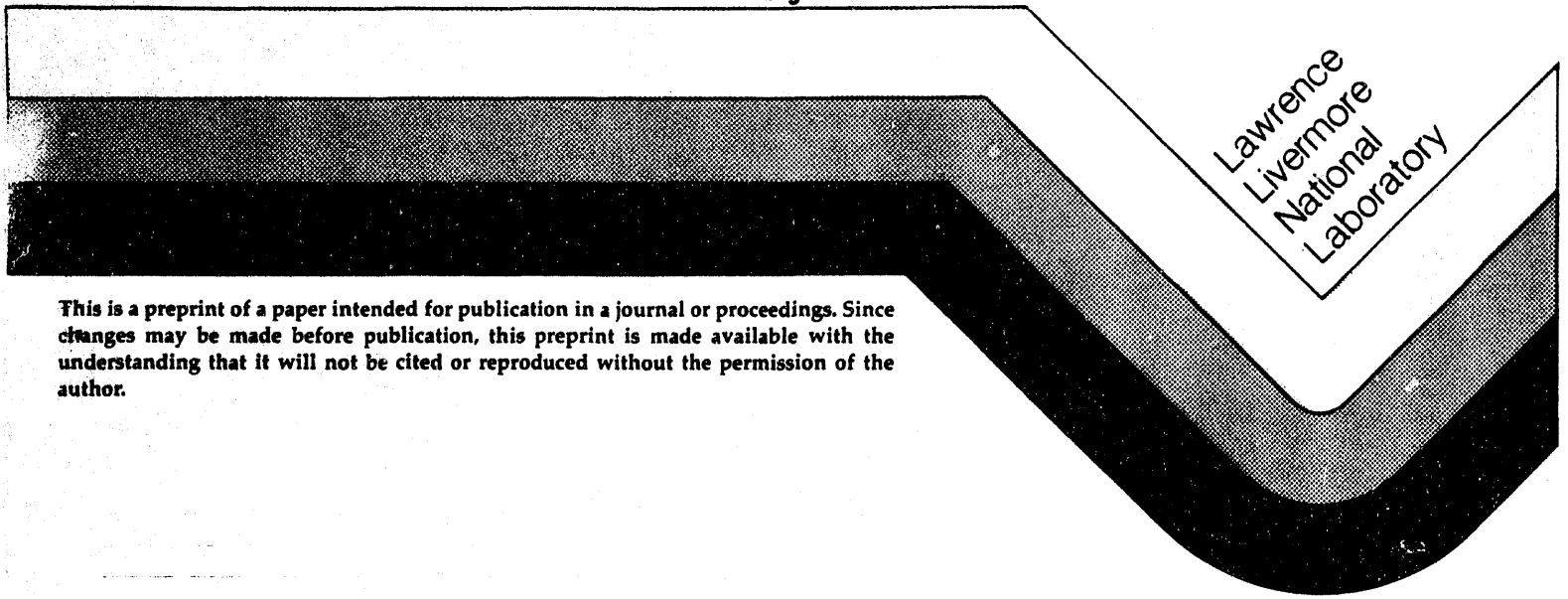
UCRL-JC- 115670
PREPRINT

**Real-Time Radiography, Digital Radiography,
and Computed Tomography for
Nonintrusive Waste Drum Characterization**

**Harry E. Martz, Daniel J. Schneberk
and G. Patrick Roberson**

**This paper was prepared for submittal to the
Nondestructive Assay and Nondestructive
Examination Waste Characterization Conference
in Pocatello, Idaho, February 14-16, 1994**

July 1994



This is a preprint of a paper intended for publication in a journal or proceedings. Since changes may be made before publication, this preprint is made available with the understanding that it will not be cited or reproduced without the permission of the author.

MASTER

DISTRIBUTION OF THIS DOCUMENT IS UNLIMITED

ee

DISCLAIMER

This document was prepared as an account of work sponsored by an agency of the United States Government. Neither the United States Government nor the University of California nor any of their employees, makes any warranty, express or implied, or assumes any legal liability or responsibility for the accuracy, completeness, or usefulness of any information, apparatus, product, or process disclosed, or represents that its use would not infringe privately owned rights. Reference herein to any specific commercial products, process, or service by trade name, trademark, manufacturer, or otherwise, does not necessarily constitute or imply its endorsement, recommendation, or favoring by the United States Government or the University of California. The views and opinions of authors expressed herein do not necessarily state or reflect those of the United States Government thereof, and shall not be used for advertising or product endorsement purposes.

REAL-TIME RADIOGRAPHY, DIGITAL RADIOGRAPHY, AND COMPUTED TOMOGRAPHY FOR NONINTRUSIVE WASTE DRUM CHARACTERIZATION

Harry E. Martz, Daniel J. Schneberk, and G. Patrick Roberson
Nondestructive Evaluation Section, L-333
Lawrence Livermore National Laboratory
P.O. Box 808, Livermore, CA 94551, USA

ABSTRACT

We are investigating and developing the application of x-ray nondestructive evaluation (NDE) and gamma-ray nondestructive assay (NDA) methods to nonintrusively characterize 208-liter (55-gallon) mixed-waste drums. Mixed wastes contain both hazardous and radioactive materials. We are investigating the use of x-ray NDE methods to verify the content of documented waste drums and determine if they can be used to identify hazardous and non-conforming materials. These NDE methods are also being used to help waste certification and hazardous waste management personnel at LLNL to verify/confirm and/or determine the contents of waste. The gamma-ray NDA method is used to identify the intrinsic radioactive source(s) and to accurately quantify its strength. The NDA method may also be able to identify some hazardous materials such as heavy metals. Also, we are exploring techniques to combine both NDE and NDA data sets to yield the maximum information from these nonintrusive, waste-drum characterization methods. In this paper, we report on our x-ray NDE R&D activities, while our gamma-ray NDA activities are reported elsewhere in these proceedings.

We have developed a data acquisition scanner for x-ray NDE real-time radiography (RTR), as well as digital radiography (DR), and/or transmission computed tomography (TCT) along with associated computational techniques for image reconstruction, analysis, and display. We are using this scanner to acquire data sets of mock- and real-waste drums at Lawrence Livermore National Laboratory (LLNL). In this paper, we discuss some issues associated with x-ray imaging, describe the design and construction of an inexpensive NDE drum scanner, provide representative DR and TCT results of both mock- and real-waste drums, and end with a summary of our efforts and future directions. The results of these scans reveal that RTR, DR, and CT imaging techniques can be used in concert to provide valuable information about the interior of low-level-, transuranic-, and mock-waste drums without opening them.

INTRODUCTION

Characterization of mixed (radioactive and hazardous) wastes requires that the identity and strengths of intrinsic radioactive sources be determined accurately and that all hazardous (e.g., heavy metals, volatile organic compounds—VOCs—and non-VOCs) and non-conforming materials (e.g. free liquids, sharp objects, particulates, and pressurized containers) be identified.[AND91] We are developing both nondestructive evaluation (NDE) and assay (NDA) methods to meet some of these characterization requirements. The NDE methods include x-ray real-time radiography (RTR), digital radiography (DR), and transmission computed tomography (TCT), while the NDA method is gamma-ray active (A) and passive (P) computed tomography (CT). Here we describe only the NDE waste-drum characterization research and development (R&D) activities within the NDE Section at the Lawrence Livermore National Laboratory (LLNL). Our NDA activities are described elsewhere in these proceedings.[ROB94]

RTR portrays on a monitor screen x-ray images of a waste drum in real time (video frame rates, i.e., 1/30-sec per image) to verify content codes and site-specific item description codes (IDC). RTR can also be used to identify nonconforming materials (free liquids, pressurized containers, etc.). DR portrays images similar to RTR, however, not in real time. Typically, a DR image is of better quality (higher signal-to-noise) than a RTR image because several video

frames are averaged, or the image is acquired over many frame times, to produce a single radiographic image. The DR images can be digitally manipulated on a computer and, if acquired over many angles around the waste drum, used to reconstruct TCT images.

Standard RTR and DR yield two-dimensional (2D) images or projections onto which three-dimensional (3D) information about the object has been projected (see middle of Figure 1). Usually, the 2D RTR images are adequate in the determination of non-conforming materials contained within the waste drum. In addition, qualified operators often use this information to verify the drum's contents, to list any discrepancies for a given IDC, and to quantify by weight the materials/items according to specific categories that make up the contents of a waste drum.[HAI94] For example in the Waste Isolation Pilot Plant (WIPP) and Idaho National Engineering Laboratory (INEL) Bin program, there are several categories of interest: (1) cellulose—this includes paper, wood, cloth and HEPA filters; (2) other organics, e.g., resins, oils, solvents and organic sludges; (3) plastics including bags, liners, and wastes; (4) rubber; (5) corroding metals—specifically steel and aluminum; (6) noncorroding metals, e.g., lead, tantalum and copper; and (7) solid inorganics—examples include glass, ceramics, graphite and vermiculite. The operator lists a best guesstimate of the weight for each category determined from analysis of the RTR data.[HAI94]

The RTR weight determining technique is difficult and very subjective even for simple waste drum matrices, since RTR is a measure of the exponential of the attenuation times path length, $\exp(\mu\ell)$, it is difficult to correlate this to and quantify the weight for the categories of interest. Techniques are under development by Allemeier, et al.[ALL94] to more quantitatively analyze the RTR data by digitizing the data before data analysis. This reduces the subjectiveness of the RTR data analysis. However, it still is difficult to extract the quantitative information, and is at best a rough approximation of the volumetric data provided by CT. For drums with complex, heterogeneous-waste matrices, the superposition of features within the waste drum can hide crucial information and this makes it even more difficult to quantify. However, TCT can retrieve true 3D information (see Figure 1).

Three dimensional (3D) TCT images nonintrusively provide exact locations, dimensions, and volumes (Figure 2) of all external and internal features—larger than the spatial resolution of the TCT system—within the waste drum. For tomographic imaging, the exponential and path length, ℓ , are computationally accounted for and the data is purely attenuation, μ ,—a function of volume density, atomic number, and energy—for the volume element size imaged. Even when not filled to capacity, 208-liter waste drums can require substantial energies for adequate x-ray penetration. As others have shown, at higher energies, attenuation is a strong and almost linear function of material density.[REI92, BER90] Obtaining the volume and the density from the CT reconstructed data provides a means for calculating the weight of included waste items in a more automated and objective manner. CT scanners can be obtained commercially in a number of configurations, each involving different price/performance implications. Surprisingly, few of these scanners include an RTR capability. At the same time, an RTR system can be fielded for a minimal cost, but with certain implications for CT inspection performance. We seek to explore the limits of the RTR, DR and 3D TCT modality for inspecting waste drums, using an inexpensive RTR system as the base system for acquiring data.

Our initial objective for designing and constructing such a system was to characterize representative LLNL drums that contain real-waste items, and use this information to design and construct a waste drum with clean—nonradioactive and nonhazardous—waste items. This mock-waste drum of clean-waste items was scanned by the NDE system and is being used to investigate the performance of this system and will be used in the study of the performance of the active and passive computed tomography (A&PCT) drum scanner. We also used this NDE drum inspection system to aid LLNL waste certification program (WCP) and hazardous waste management (HWM) personnel in the characterization of legacy wastes and to help design a dedicated LLNL RTR waste drum inspection system. Once constructed, the x-ray RTR/DR/TCT NDE system was used to scan several LLNL generated low-level-, transuranic- and mock-waste drums. Representative results for each category of waste are presented below.

In addition to our NDE efforts for waste characterization, most major Department of Energy (DOE) waste generator sites (e.g., INEL, LANL, ORNL, RFP, and WSRC)* have the capability to perform RTR inspections of real-waste drums.[WES94] However, at this time, LLNL is the only site that has an operational capability to scan real-waste drums using x-ray TCT.[MAR93] Recently we began a collaborative effort with Bio-Imaging Research, Inc. (BIR) to further develop NDE and NDA instruments to be housed in a mobile trailer to characterize real wastes.** Roney, et al. at INEL are working with Scientific Measurements Systems, Inc. (SMS) to upgrade an existing linear-array TCT scanner to be able to inspect real-waste drums.[GAL94, RON94] To date all x-ray TCT scans, except those obtained at LLNL, have been of mock-waste drums. Examples of representative TCT scan results of mock-waste drums by U.S. industrial CT vendors are given by Bernardi et al. [BER92, BER94] and Steude, et al. [STE93, STE93a, STE93b]. In addition to the U.S. efforts, we are aware of the work by Plummer et al. in England,[PLU94] and Reimers, Illerhaus, et al. in Germany [REI92, ILL89] to use x-ray NDE methods to scan waste drums. The x-ray TCT technique presented in this paper differs from the others in that we are using 2D or area-array detectors, while the others only consist of 1D or linear-array detectors.†

This paper will accomplish four tasks: (1) describe the inexpensive NDE system fielded at LLNL; (2) provide detail on the performance of the system for waste-drum characterization; (3) explore some of the advantages of 3D imaging for characterizing heterogeneous waste matrices; and (4) discuss future NDE activities to characterize wastes at LLNL. Before we do this we first think it is useful to briefly discuss the fundamentals required for x-ray imaging.

X-RAY IMAGING BACKGROUND

Conventional x- or gamma-ray imaging measures the effect of an object on an incident beam of penetrating radiation. For NDE methods using RTR, DR and TCT, the data measured are related to the energy deposited through a signal that is a function of x-ray photon intensities for both the incident and transmitted beam. The transmitted beam reflects the attenuation caused by an object within the incident beam. There are a number of ways to configure source, object/manipulator, and detector, different choices in sources and detectors, and each combination presents distinct advantages and disadvantages for the inspection of waste drums. We have found a simple 'accounting' model to be useful in tracking possible sources of x-ray fluence and for describing the intrinsic properties of the drum scanner we have constructed. Also, this model provides a means for characterizing the differences between the different choices in source-detector combinations.

Regardless of the detector, a 2D area in 3D space which is illuminated by an x-ray source can be said to contain a number of different types of fluence. Considering this area will be measured or recorded in a transmission image and result in a given picture element or pixel value, the following equations list the possible sources of radiation which compose such a measurement:

$$N_T(E, \mathbf{d}, \theta) = N_P(E, \mathbf{d}, \theta) + N_S(E, \mathbf{d}, \theta) \quad (1)$$

$$N_S(E, \mathbf{d}, \theta) = N_{Sbk}(E, \mathbf{d}) + N_{Sobj}(E, \mathbf{d}, \theta) \quad (2)$$

$$N_{T0}(E, \mathbf{d}) = N_{P0}(E, \mathbf{d}) + N_{Sbk}(E, \mathbf{d}) \quad (3)$$

* LANL—Los Alamos National Laboratory; ORNL—Oak Ridge National Laboratory; RFP—Rocky Flats Plant; WSRC—Westinghouse Savannah River Company.

** This work is being performed under DOE Program Research and Development Announcement (PRDA), contract number DE-AC21-93MC-30173; preliminary DR and TCT results are described in a paper by Bernardi and Han at Bio-Imaging Research, Inc.[BER94]

† It is useful to mention that recently INEL has begun working with SMS to develop an area-array detector based x-ray TCT scanner to inspect waste drums. This effort is in the design stage.[RON94a, STE94]

where:

- $N_T(E, \mathbf{d}, \theta)$ - the total number of photons transmitted through an object and arriving at detector position \mathbf{d} with the object at rotational angle θ , for single energy E .
- $N_P(E, \mathbf{d}, \theta)$ - the number of 'primary' photons arriving at detector position \mathbf{d} with the object at rotational angle θ for single energy E . These photons traveled from source to detector along trajectories consistent with the source beam shape.
- $N_S(E, \mathbf{d}, \theta)$ - the number of scattered photons arriving at detector position \mathbf{d} with the object at rotational angle θ for single energy E . These photons have scattered into detector position \mathbf{d} from two sources, adjacent ray-paths in the object, and outside scatter in the particular technique.
- $N_{Sbk}(E, \mathbf{d})$ - the number of background scattered photons within the detector position \mathbf{d} at single energy E . These photons are scattered into a detector from either the overall detector configuration (e.g., leakage radiation from shielding and fixturing) employed and/or from the cross talk from adjacent detector elements.
- $N_{Sobj}(E, \mathbf{d}, \theta)$ - the number of scattered photons arriving at detector position \mathbf{d} with the object at rotational angle θ for single energy E . These photons have scattered into detector position \mathbf{d} from adjacent ray-paths through the object.
- $N_{T0}(E, \mathbf{d})$ - the total number of incident photons arriving at detector position \mathbf{d} with no object in the path of the beam, for single energy E .
- $N_{P0}(E, \mathbf{d})$ - the number of 'incident primary' photons arriving at detector position \mathbf{d} with no object in the path of the beam.

The primary photons, both incident, N_{P0} , and transmitted, N_P , contain the most useful information about the object. This source of fluence travels along the source distribution function from source to detector, the loss in detected energy corresponding to the changes in object density, object length, or object components. The fluence impinging on the detector from object scatter, N_{Sobj} , contains some information about volume elements adjacent to the part of the object traversed by the primary part of the beam. As such, the scattered photons can mask certain features, spreading or blurring the impact of object features across the image. Measured signal that arises from the impact of photons scattered within the detector and the detector configuration, N_{Sbk} , is another source of blur that degrades the image. This occurs by spreading the definition of features over each other to make the identification of object geometry difficult. Given these definitions, one strategy for optimizing x-ray imaging is to increase the proportion of primary beam photons while decreasing the scattered number of photons in the detected image. X-ray imaging systems become more accurate and quantitative when the primary-to-scatter ratio (N_P/N_S) is increased. For high-energy imaging, photon scatter is an important component in the final recorded image, i.e. N_S is large. Thus, many methods have been employed to reduce scatter for improved x-ray image data acquisition at medium to high energy.

Three different source-detector combinations have been regularly fielded for obtaining transmission measurements: (1) well-collimated, single-detector systems; (2) 1D or linear arrays of detector elements with different types of collimation applied; and (3) 2D, area-array detector systems. The first type of detector when configured correctly can provide nearly scatter free imaging. For a single detector arrangement, there is no scatter from adjacent detector positions, and consequently no scatter within the detector package itself. Object scatter is reduced by collimation at the source and in front of the detector, however object scatter functions are reasonably forward peaked and can cause some small blurring for any detector aperture. The beam used to image the object is truly parallel, and the effect of the finite size of the source spot (source unsharpness) is not involved. Scatter can be nearly eliminated by using energy discriminating detectors and radioisotope sources, thus providing a pure primary-beam,

transmission measurement.[MAR91, ROB91] The price of this high-fidelity imaging system is long scan times, which can be substantial for a single radiograph or a single CT slice (or cross-sectional image), not to mention the acquisition of multiple slice data for volumetric (or 3D) imaging.

Linear-array detectors are the most popular alternative for commercial CT scanners. The source is usually collimated to produce a fan-beam of x-rays and the detector has a slit collimated aperture. Thus, scatter within the detector medium, and object scatter are reduced to a 1D problem for these types of CT systems. As shown elsewhere, slit collimation improves the primary to scatter ratio considerably.[JOH82] When the detector arrays are configured with intra-detector collimation (or septa) both object and detector element-to-element scatter is reduced in the measured data. High-brightness scintillating materials (e.g., plastics, crystals, or glass) and fast photodiodes have been shown to provide high-quantum-efficiency x-ray detection, making the most of the fluence that emerges from the collimation. In addition, these detectors measure a substantial dynamic range (from 16 to 21 bits) for the scintillator/photodiode combination and are commercially available. For the linear-array detector arrangement, source-spot size (or unsharpness) is also a determinant of image fidelity, and can increase the total blur of the system. Linear-array-based CT scanners provide fast, high-performance, high-fidelity x-ray imaging. As shown by different CT scanner manufacturers, linear-array detectors can generate high-quality CT reconstructed images of the object attenuation function.[STE93a, TON92, BER90] Perhaps the only disadvantages are the detectors small-subtended solid angle and the increased difficulty for acquiring data for 3D reconstructions. Since the detector is one dimension in extent, the object has to be translated through the array for every rotational view, or translated after every set of rotational views per slice acquired. The result is a greater reliance on object positioning hardware and somewhat longer 3D CT scan times than 2D area-array detectors for most fielded arrays.

Area-array detectors generate data for 3D or volumetric cone-beam image reconstruction algorithms, but include the impact of both object scatter and scatter from within the detector package. For the area-detector arrangement, source spot size is also an important factor in determining image fidelity. Recent advances in scintillating glass formulation and fielding have increased the spatial resolution obtainable with simple scintillator/camera x-ray imaging systems. We have been able to obtain spatial resolutions down to 20-25 line-pair per mm (lp/mm) at low (~160 keV-peak) to medium (450 keV-peak) energies, and as low as 5-6 lp/mm at high (4 and 9 MeV-peak) energies. Our results are consistent with findings published elsewhere.[PLA91, PLA90]. However, the lack of physical detector collimation (Figure 3) leaves the different sources of blur within the imaging chain. There are a number of strategies for remediating the effects of scatter within the detector (referred to as veiling glare), lessening the proportion of object scatter through source-object-detector geometry, and minimizing source unsharpness with x-ray de-magnification. Unfortunately, the procedures for controlling the different sources of image degradation are not mutually attainable. The dynamic range is usually limited by the camera used and is typically 8 to 16 bits. We have not performed the necessary experiments to establish the limits of these scintillator/camera systems. But are pursuing this in future work.

It has been our experience that area-array detector based CT systems can provide flexible 3D imaging and are straightforward to field.[MAR93a, MAR92, MAR91a] However, these systems present a number of important challenges for aligning system components before data acquisition and for configuring a particular application inspection. We have designed and assembled scanners that have an adjustable distance between all three x-ray imaging components (i.e., source, manipulator, and detector). Most of these scanners also have a variable field of view. This enables us to apply these scanners to investigate many different x-ray inspection problems. However, at the same time this flexibility takes time to align the system components and sometimes results in artifacts due to misalignment. Therefore, we have developed algorithms to determine the misalignments such as center-axis-of-rotation and midline offsets.[AZE90] These algorithms have been very useful in decreasing artifacts due to component misalignment, but we do not imply that a misaligned scanner should be fielded for any x-ray inspection problem.

Following others for example Seibert et al.,[SEI85] we have shown that to first order the N_{Sbk} component of the scattered photons is spatially invariant and can be minimized or reduced by deconvolution. Using the data from our systems, we have obtained reasonable image restoration from the application of Lorentzian shaped point spread functions (PSFs), which can be deconvolved from the 2D detected image or the sinogram (see Figures 4 and 5) using constrained Weiner techniques. This deconvolution scheme reduces a large proportion of N_{Sbk} and thus improves the spatial and contrast resolution performance of the 2D radiographic image or the final reconstructed image. However this comes at the cost of increased noise.

The N_{Sobj} component is typically not spatially invariant and is more difficult to reduce computationally. The proportion of scatter per-pixel varies with the object function, with the path length of the beam path through the object, and the electron density of the object material. Consequently we have found object scatter remediation through deconvolution or subtraction less than satisfactory for complicated objects. For 2D detectors we attempt to reduce the effects of scatter by counterbalancing the object-to-detector distance, the cone angle, and the magnification. [LIG93] The nature of this balancing act is as follows, scatter is reduced by increasing the object-to-detector distance and/or cone angle. However, this strategy eventually results in high object x-ray magnification that degrades the image through an increase in blur due to source unsharpness. High-energy sources usually possess substantial source-spot sizes (2 mm or larger) and a point is quickly reached where the gains in image fidelity due to scatter reduction schemes are overwhelmed by source-spot blur. Our strategy is simply to keep source unsharpness less than a pixel at the center of the object, and do as well as possible with object-to-detector distance and cone angle with that constraint.

In summary, we suggest the following x-ray imaging strategies. For N_{Sbk} , we advocate a deconvolution strategy for remediating detector blur. For N_{Sobj} , we attempt to explicitly manage the trade-off between object magnification required to minimize source unsharpness and increased object-to-detector distances for scatter reduction. Within these constraints we attempt to obtain as large a cone angle as possible for further scatter control. We illustrate these principles in the parameters (Table 1) used to characterize the waste drums presented in this paper.

NDE WASTE-DRUM CHARACTERIZATION SYSTEM

We have designed and constructed a high-energy x-ray transmission imaging system for acquiring RTR, DR, and CT data of full-scale, 208-liter waste drums. RTR, DR and CT systems contain four major components: (1) x-ray source; (2) object manipulator; (3) detector; and (4) data acquisition and preprocessing, image reconstruction and analysis computer(s). It is important to emphasize that this system was designed and constructed in a manner to keep the costs at an absolute minimum. To meet this end, we chose to use available system components.

The components used are not necessarily the best choice of equipment to characterize waste drums, however, they were available and sufficient to actually obtain RTR, DR, and TCT data sets that meet the waste-drum characterization requirements stated above. These components include: (1) a 4-MeV linear accelerator source; (2) a three-axis (translational, elevational, and rotational) drum manipulator; (3) an area-array detector; and (4) two computers. A schematic diagram of the NDE system designed and constructed to inspect waste drums is shown in Figure 6. A photograph of the system is shown in Figure 7. The accelerator source (4 MeV, 420 rads/min. @ 1 m) is higher in energy than one would prefer, however, we found that we were able to penetrate all the drums scanned and produced images with enough contrast to determine the drum's contents. The manipulator is sufficient to handle wastes drums up to 300 kg and elevate them through 30.5 cm. This allows the inspection of most waste drums at LLNL.

The detector is the large-area-array, x-ray imager that was designed and constructed to investigate the build up of slag in a Titan solid rocket motor upgrade by RTR and DR imaging during a static test firing.[DOL94] This detector combines a 2D scintillator and bending mirror lens coupled to a video-frame-rate camera. The scintillator consists of 9 inexpensive Trimax-12B ® intensifier screens (DuPont NDT, McKinney, TX) configured to provide a 107-cm wide by

130-cm high imaging area. The field-of-view provided by the camera and optics is 74-cm wide by 90-cm high, large enough to cover the entire width of a 208-liter drum. Thus we use third generation (rotate only) CT scan geometry data acquisition. However, the 90-cm high field of view can only acquire about two-thirds the height of the drum. In order to image the remaining third of the drum it must be elevated and rescanned. Typically this was not required since the top third of most of the real-waste drums we inspected were empty. The mirror, lens, and camera (intensified-CCD—ICCD or cooled variable-integration-rate CCD) are off-the-shelf items. ICCD cameras provide high gain for low-light-level scintillation screens, but can be expensive. Variable integration-rate CCD cameras (8-bit) are inexpensive and provide frame integration rates that range from 1/30 second to several minutes. Cooling these cameras significantly reduces electronic noise. An illustration of the layout of the detector is shown in Figure 3. The system components used are shown in Figure 6. A PC compatible computer was used to acquire and control the data acquired, while a Silicon graphics computer was used in image preprocessing, reconstruction, and data analysis.

In the RTR mode the data are acquired and stored directly onto a video tape. For the DR or TCT mode of data acquisition, the data are digitized and stored on a computer hard disk. The quantity that is recorded in each 2D image at each x, z coordinate of the detector plane is the intensity, I , transmitted through the thickness of the object. A representative 256-frame-summed unprocessed DR image is shown in Figure 8 (left). By increasing the exposure time (frame summing) we are suppressing the noise and effectively increasing the dynamic range of our 8-bit camera. We have not established the details of frame summing on the final dynamic range, but have shown improvements over simple averaging. The DR image is usually further processed to remove the nonuniform intensity pattern of the x-ray source, correct for non-square detector elements within the camera, and to extract the area within the image that is of interest. The nonuniform-intensity pattern of the x-ray source is removed by calculating the natural log (\ln) of the ratio I_0/I for the entire DR image, where $I_0 = \epsilon N_T \tau_0$, and $I = \epsilon N_T$; ϵ is the efficiency of the detector. The quantity $\ln(I_0/I)$ is equal to x-ray attenuation, μ ,* times path length, ℓ , and is sometimes called a ray sum. It is useful to note that a ray sum acquired at a single energy is analogous to a simple gamma-ray transmission gauge. The non-square detector elements are corrected for by resampling the image. An example of a processed DR image is shown in Figure 8 (right).

For TCT, several digitized radiographic images of the drum are recorded at many different angles. The reconstruction algorithms require line integrals, also called ray sums, for many ray paths through the object. Each DR or projection image provides the data necessary for CT image reconstruction, however, first it must be processed to determine ray sums as described above for the DR data sets. Depending on the half-cone angle of the NDE system the tomographic images are generated from these preprocessed projections by either of three different image reconstruction methods.[AZE90a] For small half-cone angle ($<1^\circ$) or parallel-beam data sets, the image is reconstructed using a filtered backprojection (FBP) algorithm into a single 2D cross-sectional image or tomographic slice. For medium half-cone angle ($<1-3^\circ$) or fan-beam data sets, the image is reconstructed using a convolution backprojection (CBP) algorithm. These algorithms account for the angle only in the dimension perpendicular to the center-axis-of-rotation and also results in a single 2D image or data set. From either of these algorithms, multiple individual slices are combined (or rendered) in a computer to generate a full 3D data set. For larger half-cone angles ($>3^\circ$) data sets, the image is reconstructed using volumetric cone-beam algorithms. These algorithms account for the half-cone angle and result in a complete 3D volume image or data set.[RIZ91, KUD90, SMI85, FEL84] For any case, the quantity reconstructed is the attenuation value for some volume element, or voxel, at location x,y,z within the object.[BAR81] The voxel size and clarity are defined by the data acquisition (or scan), preprocessing, and image reconstruction parameters used.

* In this paper, μ represents the absolute linear attenuation coefficient in cm^{-1} units, while μ_R represents a relative measure of the attenuation coefficient.

EXPERIMENTS

We have acquired multiple sets of data to characterize both real- and mock-waste drums. These data sets typically include all three NDE imaging methods (i.e., RTR, DR, and TCT). Here it is difficult to show the RTR data sets, since the main advantage of RTR is in its ability to show motion in real time. Thus, we chose not to show any still RTR images via a photograph from a video monitor or a digital image of a single-video frame. However, we do show representative DR and TCT images for several of the waste drums inspected. For these data sets a typical scan consisted of the data acquisition, preprocessing, and image reconstruction parameters shown in Table 1. Below we present representative data sets acquired and reconstructed for each of the three waste categories—low-level, transuranic, and mock wastes.

We scanned two low-level-waste (LLW) drums and used this information to help design and construct a mock-waste drum.[CAM94] These drums were chosen to be representative of LLW generated by the Nuclear Chemistry Division at LLNL. The two drums chosen differed by their waste matrix. One contained mainly glass and the other metal. Representative digital radiographic images for the glass- and metal-matrix drums are shown in Figure 9 and 10, respectively. The data for each drum was reconstructed to reveal further interior details and representative tomograms for each are shown in Figure 11.

We scanned five transuranic (TRU) waste drums. These drums were scanned to help WCP personnel in determining the actual content of these so called legacy TRU waste drums. In addition, we used this information to help design and construct a mock-waste drum.[CAM94] Some of these drums consisted of matrices with only a few waste items while others had several waste items. The drums with only a few items were easily identified by both RTR and DR and thus we typically did not need to obtain tomographic data to characterize these types of drums.* One representative example is shown in Figure 12. On the other hand, the drums that contain a complex matrix of several waste items are more difficult to characterize with only radiographic data (Figure 13); thus we used TCT to reveal further interior details as shown in Figures 1 and 14. This volumetric tomographic data helps simplify data analysis to most accurately characterize the rather complex matrices contained within waste drums.

Lastly, we scanned several mock-waste drums that are being used to understand the performance of the A&PCT waste assay scanner. In addition, these drums are useful in understanding the performance of the NDE system. Here we discuss only one mock-waste drum. This drum and its contents are described in a paper by Camp, et al. published in these proceedings.[CAM94] Representative digital radiographic and transmission CT images of this drum are shown in Figures 15 and 16, respectively. The resultant DR and TCT data are analyzed as described in detail below for most of the drums scanned by the NDE system.

RESULTS AND DISCUSSION

For NDE high-energy imaging applications, there are various ways of analyzing the data. With the 4-MeV x-ray source and current integrating area-array detector. The real-time and digital radiographic images are an indirect or relative measure of the integral of the exponential of the relative linear attenuation coefficient, μ_R , over the ray path length, ℓ .** This integration makes it difficult to interpret the radiographic results (Figure 1). The tomographic images result in a relative measure of attenuation, μ_R , only—the exponential and integral over ℓ is eliminated during image reconstruction. It is important to note, that the attenuation value is integrated over the x-ray source energy spectrum as well for both the radiographic and tomographic data sets. Given the 4-MeV LINAC spectrum, we expect the differences in μ_R to be mainly a function of differences in material density. We have attempted to measure these spectra using nuclear

* Sometimes it is useful to acquire and reconstruct regions-of-interest even with these somewhat simple waste matrices. The TCT images reveal details of additional interest not obtainable by RTR or DR alone and can be used to provide more quantitative data.

** In the text the integral of the exponential of the relative attenuation coefficient, μ_R , over the ray path length, ℓ is sometimes referred to as a ray sum, $\ln I_0/I$, or $\mu_R \ell$, all of which represent the same parameter.

spectroscopy methods. Our attempts have not been very successful. Given this and the uncertainty as to the actual x-ray spectrum produced by a high-energy LINAC sources, we refer the reader to results published elsewhere.[VAR88]

Of the several ways to qualitatively and quantitatively analyze these data, the easiest is to visually compare the fluctuations of the integral of the x-ray attenuation over the ray path within each radiographic image and from image to image. For tomographic images, it is a comparison of μ_R only. Gross anomalies are thus easily identified. To determine a slightly more quantitative measure within an image and between images, a gray scale is used to quantify the gray tones to changes in $\mu_R \ell$, and μ_R for radiographic and tomographic data, respectively. A more detailed analysis would be to study the resulting 1D profiles (or line outs) and histograms of regions within the waste drum. This information may reveal further details about the actual waste items disposed by the waste generator. 1-D profiles of the data can also be plotted to reveal small variations in attenuation from image to image and within each image. This technique is useful in a detailed analysis of small pixel-to-pixel changes in the relative attenuation map. Histograms of the data reveal the range and amount of different attenuation that is related to the type of waste items. In the text we quote the relative attenuation values in inverse pixels.

We discuss the results of the mock-waste drum first, since it contains waste items that are well characterized and could be used to understand the performance of our NDE system. In addition, this can reveal the methods that are useful in extracting various information about the drum and its contents. The mock-waste drum constructed to represent LLNL wastes consisted of three equal sections by volume.[CAM94] The top and middle sections contain LLW with low-density combustibles and medium-density clean-waste items, respectively. The bottom section contains representative clean TRU-waste items of medium density. Three aluminum tubes are inserted along the length of the drum to allow access for passive radioactive sources to be placed among the waste matrices. Each section was separated by a Plexiglas divider. The waste items were fixed in place and foam was inserted to insure that the individual items did not move during movement of the drum. The different waste matrices and dividers are easily revealed in the DR images shown in Figure 15.

With respect to Figure 15, a preliminary analysis reveals that the integral of μ_R over ℓ , range from highest to lowest from the bottom, through the middle, to the top. This is expected given the description of the waste drum sections above. Further analysis reveals that the bottom section has small regions where the ray sum or $\mu_R \ell$ values are quite high ~ 2.4 —bottom middle regions of the images shown in Figure 15. Some of the individual items placed within the waste drum are discernible. For example in the bottom section of the DR image some detailed inspection and prior knowledge of the contents reveals the scrap metal channel, warning light, Plexiglas can, oil filter, and metallic-flexible hose. In the middle section, the items are packed to a higher density and only the concrete and one to two of the three 4-liter (1-gallon) paint cans are discernible, while in the top layer it is difficult to identify any of the combustible items. However, one would easily be able to determine if a nonconforming item, such as a screw driver or pair of scissors, was placed among the combustible matrix. For further analysis of the DR images, line outs and histograms are shown in Figures 17 and 18, respectively. These plots reveal some additional quantitative data about the $\mu_R \ell$ values for the particular waste matrix sections. For example, the 1D profiles and histograms selected reveal the fact that the $\mu_R \ell$ values range from high to low with the waste items in the bottom to top. However, due to the integral of μ_R over the path length ℓ it is difficult to extract any additional details.

For further details and to better understand the individual items contained within these complex matrices, we acquired and analyzed a complete 3D volume tomographic data set. Representative cross-sectional images within each waste-matrix section are shown in Figure 16. In all three images, the aluminum tubes are easily revealed and the details of the individual waste items are more clearly discernible. For example, in the top section the pieces of wood, some paper cartons and plastic bottles are visible, in the middle section all three paint cans, two full and one half-empty, are shown. For the tomographic slice shown, the middle can is empty and the outer two cans are full of material—solidified Petrosset, diatomaceous earth and water. In addition, other items (e.g., the scrap metal parts and the piece of concrete) are discernible,

however, most of the other individual items are difficult to interpret by analysis of just this one 2D cross-sectional image. In the bottom section for the tomogram shown, most of the items placed within this TRU waste section are discernible—e.g., the warning light, Plexiglas can, oil filter, and metallic flexible hose. However, some items, e.g., the brackets are difficult to identify. Analysis of the CT data given in Figures 19, 20, and 21 reveals that the locations of the various waste items determined by the multiple tomographic data correlate well with the placement of the various items fixed within the mock-waste drum.[CAM94] Rendering images of the individual tomograms into a 3D image can be used to more clearly identify some of the individual waste items as shown in Figure 22.

Plots for selected 1D profiles within the individual sections are shown in Figures 23-25. These plots reveal further details of the individual waste items and their location within the waste drum. With respect to Figure 23, most of the combustible items have a relative attenuation value near 0.0007. However, there are a other items with attenuations around 0.0018 that are higher in attenuation value than the Al tubes. These are the CYNROC pellets and assorted metallic pieces. waste items placed within the low-density, combustibles section. The profile labeled s0 reveals the attenuation due to the 3 aluminum tubes. Note that the wall of the tube near the drum wall is not distinguishable from the drum wall, also the relative attenuation decreases as a function of distance within the drum. This is attributed to the well known CT cupping artifact—beam hardening and scatter. With respect to Figure 24, the profiles s0 and s1 reveal details of the various material attenuations and the extent of cracking and voids with the paint cans. With respect to Figure 25, the high attenuation values near, 0.009, are attributed to the steel brackets while the attenuation values near 0.0040 are attributed to the walls of the warning light and the connectors for the flexible hose all of which were placed within this section of the mock drum.

Histograms for the individual tomograms (see Figure 16) of the mock-waste drum sections are shown in Figure 26. Histograms reveal the distribution of attenuation values within the drum sections and the amount by volume (Figure 2). For the drum data presented in this paper, each pixel represents the relative attenuation averaged over a volume of $\sim 2 \times 2 \times 2$ or 8 mm^3 . Analysis of this data reveals the different attenuation distributions that are related to the different materials that make up the waste items. With respect to Figure 26, the large peaks near an attenuation value of 0 are due to air both inside and outside the object. The peaks just greater than 0, shoulders in each of the three histograms, are most likely due to very low-attenuating items, e.g., the foam used to fill the drum void space. Further analysis of the low-density, combustible, LLW histogram reveals two additional peaks near 0.0006 (paper, plastic and wood) and 0.0013 (other higher attenuating items). The medium-density, LLW section contains three distinct peaks at 0.0006 (low attenuating items and maybe scatter), 0.0015 (concrete and petroset), and 0.0026 (steel, tools, brackets and scrap metal). The TRU waste section contains one distinct peak at 0.0015, this may be attributed to plexiglass. In addition, there are data at higher-attenuation values for the medium LLW and TRU waste sections, however, the TRU section goes to the highest values near 0.007. These are the steel brackets. Overall analysis of the histogram data seems to suggest some correlation with the actual density for the individual sections—i.e., the total number of pixels increase at higher attenuation from the top to the bottom sections of the mock-waste drum. This is what is expected and is thus very encouraging.

Histograms for selected 3D volumes of the mock-waste drum sections are shown in Figure 27. The histogram for the low-density LLW matrix volume data set has three distinctive peaks at attenuation values near those shown in the low-density LLW single-tomographic histogram (Figure 26). This suggests that the single tomogram shown in Figure 16 (left) is representative of the overall waste matrix (Figure 19). With respect to Figure 27, the LLW medium-density volume histogram has only two distinctive peaks. The prominence of the peak at 0.0015 is much higher than the LLW medium-density single-tomographic peak at 0.0015 shown in Figure 26. Analysis of the volume data set and tomograms shown in Figure 20 suggests that this peak is due to the total volume of the piece of concrete. It is not very dominant in the single-tomographic histogram since only a portion of the piece of concrete is within the slice plane shown in Figure 16 (middle). However, it does take up a considerable portion of the LLW matrix as revealed in Figure 20. Overall, the volume histogram for the TRU waste matrix is very

similar to that of the single-tomographic histogram. This suggests that the single-sonogram shown in Figure 16 (right) is representative of the overall attenuation for this waste matrix (Figure 21).

Overall the RTR, DR, and TCT data sets reveal considerable details of the individual waste items contained within the mock-waste drum. However, it is useful to point out that prior knowledge of the actual waste items made it easier to interpret the data sets. Now, we apply these various techniques and analysis methods to real-waste drums. For these drums we did not have any prior information before analysis of their data sets. Afterwards we utilized any manifests, showed and discussed our results with WCP, HWM and waste generator personnel. We found all of this useful in interpreting the data sets.

Two low-level waste drums were inspected by the NDE system. The DR images are shown in Figures 9 and 10, for the glass- and metal-matrix drums, respectively. These images reveal some of details for the items contained within each drum. For example in the glass-matrix drum, there seems to be several glass items as well as a high-attenuation region near the center of the drum. The metal-matrix drum appears to contain several metallic items such as ring stands, rods, and a large-metal plate with several holes drilled inside it. Neither drum appears to contain any free liquids. To better understand the items contained within these drums, representative tomograms are shown in Figure 11. In the slice plane chosen for the glass-matrix LLW drum individual glass items (e.g., beakers, Erlenmeyer flasks, and test tubes) as well as a bag of high-attenuating waste are clearly part of the matrix. Representative 1D profile and histogram of this tomogram are shown in Figures 28 and 29, respectively. Analysis of this data does not clearly reveal the identity of the items contained within this bag. One possibility is that it could contain a high-density packing of broken pieces of glass. With respect to the tomogram shown in Figure 11 (right), the metal matrix drum clearly shows the metal plate and other attenuating items such as metal ring stands and other metallic scrap pieces.

We scanned five transuranic (TRU) waste drums. We have found that some TRU-waste drums have only a few items that were discarded. Representative DR results for such a drum are shown in Figure 8 and 12. The DR images clearly reveal that this TRU-waste drum has a hydraulic jack inside a smaller container or drum. Drums with simple matrices as shown in Figure 12 are easily analyzed to verify or determine content identification and to determine whether they contain any nonconforming materials. A histogram for one DR image is shown in Figure 30. It is not clear as to the usefulness of histograms of DR images. However, they do show the $\mu_R \ell$ values that may be somewhat characteristic for similar content codes. Typically, for these drums tomographic imaging is not required unless there is a need to further quantify the drum contents. On the other hand some drums include many individual waste items and it is more difficult to determine by RTR or DR alone the actual drum contents and to identify hazardous and non-conforming materials that were discarded.

Digital radiographic images of a TRU-waste drum with a complex matrix are shown in Figure 1 and 13. The manifest for this drum stated that it contained crucibles contaminated with Plutonium. From the DR images it appears that the crucibles are broken and contained within several small canisters. Detailed analysis of the contents via these DR images is not as straight forward as the simple-matrix drums. Thus we acquired and reconstructed tomographic images to reveal further interior details of this waste drum as shown in Figure 1 and 14. Analysis of these images reveals a few individual bags of waste and several small canisters of different diameter are contained within this drum. Further analysis reveals the contents of the bags and small canisters. For example, the canisters contain the broken crucible pieces. The tomographic data was also rendered into multiple 3D images to generate a film loop. This film clearly reveals the internal details of this waste drum. One representative frame or 3D image for the film loop is shown in Figure 31. For further analysis a histogram of the TRU-waste drum CT volume data set was determined and is plotted in Figure 32. The histogram has several peaks. Of these peaks none are clearly resolved from the others, even though some useful information may be extracted from this data. The strongest peak is at a relative attenuation value of 0 this represents air. Two other peaks are discernible, one peak just greater than 0 that represents low attenuating items and the other at an attenuation value near 0.0022 that appears to be due to the steel-drum liner. The

broken crucibles are at an attenuation of 0.0045. The artifacts caused by beam hardening and scatter make material identification on the basis of relative attenuation value difficult.

SUMMARY

We have constructed an inexpensive fast, nonintrusive x-ray NDE system that is capable of acquiring either of three types of data: (1) real-time radiography; (2) digital radiography; or (3) transmission computed tomography. This system was used to scan several real- and mock-waste drums. The RTR mode provided the capability to see fluids and other nonconforming waste items. However, the spatial and contrast resolution of the RTR images were not as good as commercially available systems for a variety of reasons. The DR images provided more detail than RTR and can be used to characterize simple-matrix waste drums with only a few images.

The CT reconstructed volumes provided unambiguous detail on a variety of waste items and when rendered into a movie can give the user an important visualization of the waste drum contents. Items that were previously obscured in the radiographic data are imaged in their correct 3D position with the internal features revealed. The advantage of the 3D data set is the ability to obtain 2D slices in any direction through the volume for more detailed object identification. The 2D slices can be further interrogated with conventional analysis techniques (1D profiles and histograms).

The results of these scans reveal that RTR, DR, and CT imaging techniques can be used in concert and provide valuable information about the interior of low-level-, transuranic-, and mock-waste drums without opening them. These results were also valuable in helping WCP and HWM personnel verify, confirm and analyze well documented and legacy waste. However, it is not clear if materials identification can be performed in a straightforward fashion. We found a fair amount of blurring and cupping artifacts in the thick and dense matrices at 4 MeV. This accounts for a variation in the relative attenuation coefficient for a given material from drum to drum. We will continue to further calibrate our scanner in an attempt to remediate these effects.

FUTURE WORK

Due to the success demonstration of the NDE system constructed, we are getting interest from different waste generators around LLNL and from other applications—e.g., inspection of transmission casings—that require a large-imaging field of view. Thus we decided to redesign and construct a new NDE system that will be able to scan a full height of a 208-liter drum and other large items such as entire transmission casings. This system will be compatible with either a medium (320 keV-peak) to high (9-MeV) energy x-ray source. It will utilize a new designed large-area-image detector that consists of 9 3M GOS screens, a bending mirror, lens coupled to a CCD camera. The system will be somewhat transportable to scan wastes in their facilities before transporting the drum. The system is nearly completed and will go through a test and evaluation of mock drums before we transport it to scan real-waste drums. In addition to this NDE system, LLNL has designed a mobile NDE system that will be able to acquire RTR, DR, and TCT data sets of waste drums. This system will be fabricated at LLNL and used to routinely scan and analyze mixed wastes at LLNL and other sites.

Further experiments are continuing to investigate the results obtained by NDE systems to characterize wastes. The results of the different techniques (RTR, DR, and TCT) need to be more fully understood with respect to NDE waste drum characterization and how this NDE data can be coupled with the NDA techniques to maximize the characterization of wastes within the DOE complex and elsewhere as well. From our experience with these 3D data and other 3D reconstructed volumes, we are impressed by the meager resources and inadequate analysis techniques which are needed for a full analysis of the 3D data. At this point in time we see a need for more 3D automated analysis tools and better computer environments for manipulating 3D volumes. We need substantial computer resources to analyse the 3D data sets without reducing the dynamic range to satisfy memory or disk requirements. Improvements in 3D automated analysis of CT data will need to accompany any successful fielded scanner.

ACKNOWLEDGMENTS

We thank Ken Dolan for letting us use the large-area imager for this study. We want to thank Dave Camp for determining which LLW drums to characterize, Kem Hainebach for providing the TRU waste drums of interest, and Linwood Hester, Gene Ford and Derrill Rikard for setting up the RTR/DR/CT experiments and for helping obtain the empirical data. This work was partially funded by the Office of Technology Development in DOE's Environmental Restoration and Waste Management Program and performed under the auspices of the U.S. Department of Energy by the Lawrence Livermore National Laboratory under Contract W-7405-Eng-48.

REFERENCES

- [ALL94] R. T. Allemeier, D. M. Tow, and T. J. Roney, "A Digital Processing System for Conventional Real-Time Radiography," *Proceedings of the Nondestructive Assay and Nondestructive Examination Waste Characterization Conference*, Pocatello, Idaho, February 14-16, 1994.
- [AND91] B. C. Anderson and D. J. Osetek, *Nondestructive Examination and Assay System Research and Development Requirements to Meet Evolving Regulations for Transuranic and Low-Level Wastes*, draft report, Waste Isolation Pilot Plant, Carlsbad, NM (1991).
- [AZE90] S. G. Azevedo, D. J. Schneberk, J. P. Fitch, H. E. Martz, M. F. Skeate, and G. P. Roberson, "Estimation of Geometrical Parameters in Parallel-beam, Fan-beam, and Cone-beam CT Systems," *Review of Progress in Quantitative Nondestructive Evaluation*, D. O. Thompson and D. E. Chimenti, Eds. (Plenum Press, New York, 1990).
- [AZE90a] S.G. Azevedo, H.E. Martz, M.F. Skeate, D.J. Schneberk, and G.P. Roberson, *Computed Tomography Software and Standards*, Lawrence Livermore National Laboratory, Livermore, Calif., UCRL-ID-105132, February, 1990.
- [BAR81] H. H. Barrett and W. Swindell, Radiological Imaging: Theory of Image Formation, Detection and Processing, vols. 1 and 2, New York: Academic Press, 1981.
- [BER90] Richard T. Bernardi, "The Feasibility of Using Digital Radiography (DR) and Computed Tomography (CT) to Characterize Solidified Low-Level Nuclear Waste," *Proceedings on Radioactive, Hazardous, and/or Mixed Waste Sludge Management*, Knoxville TN, December 4-6, 1990; DOE SBIR Project No. 10993-90-1 Final Report, November 15, 1990.
- [BER92] Richard T. Bernardi and Robert E. Slocum, "Digital Radiography and Computed Tomography for Advanced Inspection of Solidified Nuclear Waste Containers," in *Review of Progress in Quantitative Nondestructive Evaluation*, D. O. Thompson and D. E. Chimenti, Eds. (Plenum Press, New York, 1992), pp. 1893-1900.
- [BER94] Richard T. Bernardi and Kyung S. Han, "Nondestructive Evaluation and Assay of Nuclear Waste Drums with High Energy Transmission and Emission Computed Tomography," in *Proceedings of the Waste Management '94 Symposia*, Tucson, AZ (1994).
- [CAM94] David C. Camp, John Pickering, and Harry E. Martz, "Design and Construction of a 208-L Drum Containing Representative LLNL Transuranic and Low-Level Wastes," *Proceedings of the Nondestructive Assay and Nondestructive Examination Waste Characterization Conference*, Pocatello, Idaho, February 14-16, 1994; UCRL-JC-115672, Lawrence Livermore National Laboratory, Livermore, CA, February 1994.
- [DOL94] Kenneth W. Dolan, Gary M. Curnow, Dwight E. Perkins, Daniel J. Schneberk, Bart W. Costerus, Mark J. La Chapell, Donald E. Turner, and Phinas W. Wallace, *Real-Time Radiography of Titan IV Solid Rocket Motor Upgrade (SRMU) Static*

- Firing Test QM-2*, Lawrence Livermore National Laboratory, Livermore, CA, UCRL-CR-117148 (1994).
- [FEL84] L.A. Feldkamp, L.C. Davis, and J.W. Kress, "Practical Cone-Beam Algorithm," *J. Opt. Soc. Am. A*, **1**(1984)612.
- [GAL94] S. G. Galbraith, T. J. Roney, and G. G. Streier, *DRCT Scanner Status Report*, to be published as an internal report, Idaho National Engineering Laboratory, Idaho Falls, ID (1994).
- [HAI94] S. M. Hailey, "A Comparison of Real-Time Radiography Results and Visual Characterization Results with Emphasis on WIPP WAC and TRAMPAC Compliance Issues," *Proceedings of the Nondestructive Assay and Nondestructive Examination Waste Conference*, Pocatello, ID, February 14-16, 1994.
- [ILL89] B. Illerhaus, J. Goebels, A. Kettschau, and P. Reimers, "Non-Destructive Waste Form and Package Characterization by Computerized Tomography," *MRS Symp. Proc.* **127**(1989)507.
- [JOH82] P. C. Johns and M. Yaffe, "Scattered Radiation in Fan-Beam Imaging Systems," *Med. Phys.* **9**(1982) pp. 231-239.
- [KUD90] H. Kudo and T. Saito, *JOSA*, **A7**(1990)2169.
- [LIG93] Glenn M. Light, Daniel J. Schneberk, and Fletcher Bray, "Turbine Blade Internal Structure and Defects NDE," Southwest Research Institute, San Antonio, TX, Technical Operating Report, May (1993).
- [MAR91] H. E. Martz, G. P. Roberson, D. J. Schneberk, and S. G. Azevedo, "Nuclear-Spectroscopy-Based, First-Generation, Computerized Tomography Scanners" *IEEE Trans. Nucl. Sci.* **38**(1991)623.
- [MAR91a] Harry E. Martz, Dwight W. Perkins, Stephen Azevedo, Daniel J. Schneberk, Michael F. Skeate, and George P. Roberson, *Computerized Tomography*, Lawrence Livermore National Laboratory, Livermore, Calif., UCRL-53868-90, October, 1991.
- [MAR92] H. E. Martz, D. J. Schneberk, G. P. Roberson, and S. G. Azevedo, *Computerized Tomography*, Lawrence Livermore National Laboratory, Livermore, CA, UCRL-53868-91 (1992).
- [MAR93] Harry E. Martz, G. Patrick Roberson, S. G. Azevedo, and Richard W. Ryon, "Characterization of Waste Drums Using Nonintrusive NDE/NDA Methods," *Symposium on Hazardous Materials, Identification, Handling and Management*, Arzamas-16, Russia, January 25 - February 2, 1994; UCRL-JC-115724, Lawrence Livermore National Laboratory, Livermore, CA, December 1993.
- [MAR93a] Harry E. Martz, Stephen G. Azevedo, Daniel J. Schneberk, and George P. Roberson, *Computed Tomography*, Lawrence Livermore National Laboratory, Livermore, Calif., UCRL-53868-92, March, 1993; Lawrence Livermore National Laboratory, Livermore, Calif., UCRL-ID 114541, March, 1993.
- [PLA91] R. C. Placious, D. Polansky, H. Berger, C. Bueno, C. L. Vosberg, R. A. Betz, and D. J. Rogerson, "High-Density Glass Scintillator for Real Time X-Ray Inspection," *Mats. Eval.* November, 1991.
- [PLA90] R. C. Placious, D. Polansky, E. S. Gaynor, H. Berger, C. Bueno, R. A. Buchanan, C. L. Vosberg, and R. A. Betz, "An Improved Glass X-Ray Scintillator," Final Report NWC Contract #N60530-88-C-0252, Naval Weapons Center, China Lake, CA (1990).
- [PLU94] Hugh Plummer, Rolls Royce Mateval, Derby, England, private communication (1994).
- [REI92] P. Reimers, "Quality Assurance of Radioactive Waste Packages by Computerized Tomography, Task 3, Characterization of Radioactive Waste Forms; A Series of Final Reports (1985-89) - No. 37," *Nuclear Science and Technology*, EUR 13879 EN, Commission of the European Communities, Luxembourg, 1992.

- [RIZ91] Ph. Rizo, P. Grangeat, P. Sire, P. LeMasson, P. Melennec, *JOSA*, **A8**(1990)1639.
- [ROB91] G.P. Roberson, H.E. Martz, D.J. Schneberk, and C.L. Logan, "Nuclear-Spectroscopy Computerized Tomography Scanners," *1991 ASNT Spring Conference*, Oakland, CA, March 18-22, 1991, p. 107.
- [ROB94] G. Patrick Roberson, Harry E. Martz, Daniel J. Decman, Stephen G. Azevedo and Eric R. Keto, "Characterization of Waste Drums Using Nonintrusive Active and Passive Computed Tomography," *Proceedings of the Nondestructive Assay and Nondestructive Examination Waste Characterization Conference*, Pocatello, Idaho, February 14-16, 1994.
- [RON94] T. J. Roney, R. T. Allemeier, S. G. Galbraith, and D. M. Tow, "New Developments in Radiography and Tomography of Waste Containers at the Idaho National Engineering Laboratory," to be submitted to *Spectrum* (1994).
- [RON94a] Tim Roney, Idaho National Engineering Laboratory, Idaho Falls, ID, private communication (1994).
- [SEI85] J.A. Seibert, O. Nalcioglu, W. Roeck, "Removal of Image Intensifier Veiling Glare by Mathematical Deconvolution Techniques," *Med. Phys.* **12**(1985) pp. 281-288.
- [SMI85] B. D. Smith, *IEEE Trans. Med. Imaging*, **MI-4** (1985)14.
- [STE93] John Steude, Ed Strickland, Dee Summers, and Ruben Reyes, "Nondestructive Evaluation of Radioactive Waste Drums Containing Miscellaneous Waste Forms," in *Review of Progress in Quantitative Nondestructive Evaluation*, D. O. Thompson and D. E. Chimenti, Eds. (Plenum Press, New York, 1993), pp. 2289-2296.
- [STE93a] John Steude, Jeff Anders, Richard Sporny, and Ed Strickland, "Nondestructive Evaluation of Radioactive Waste Drums Containing Cement-Solidified Liquid Wastes," in *Review of Progress in Quantitative Nondestructive Evaluation*, D. O. Thompson and D. E. Chimenti, Eds. (Plenum Press, New York, 1993), pp. 2265-2272.
- [STE93b] John Steude, Ed Strickland, and Jeff Anders, "Radioactive Waste Drum Inspection Using Computed Tomography and Digital Radiography," *WM'93 Conference Proceedings*, Tucson, AZ, February-March, 1993.
- [STE94] John Steude, Scientific Measurements Systems, Inc., Austin, TX, private communication (1994).
- [TON92] Paul D. Tonner and J. H. Stanley, "Supervoltage Computed Tomography for Large Aerospace Structures," *Mats. Eval.* **12**(1992)1434.
- [VAR88] "Characteristics of High-Energy Radiation," Chapter II in *High Energy X-Ray Applications*, Varian Corp., Palo Alto, CA (1988).
- [WES94] Bill Weston, et al., *DOE NDA/NDE Waste Characterization Instrumentation Data Base*, document in preparation by NDA/NDE Interface Working Group, Waste Isolation Pilot Plant, Waste Isolation Division, Westinghouse, Carlsbad NM (1994).

Table 1: Typical data acquisition, preprocessing, and image reconstruction parameters used to image the waste drum data shown in this paper

Data acquisition parameter	Value
• Source-to-detector distance	6 m (20')
• Object-to-detector distance	0.4 m (16")
• Half-cone angle	30°
• Source energy	4 MeV
• Source intensity	420 Rads/min. @ m
• Source Unsharpness	0.008-0.3 mm
• Number of ray sums	320
• Number of projections	301
• Projection size	320 x 420
• Number of frame averages	256
• Integration time per frame	1/30 sec.
• Total data acquisition time	1 hr. 10 min.
• Total projection data set size	84 MB
• Effective detector size	1.97 mm x 1.97 mm
• Dynamic range	8 bits
Preprocessing parameter	Value
• Ring removal	0.5 order 5
• Scatter deconvolution	Lorentzian
• Resampling to correct for uneven camera pixels	x: 1.00 y: 1.25
Image reconstruction parameter	Value
• Reconstruction algorithm used	CBP/Feldkamp
• Reconstructed image size	320 x 320 x 336
• Pixel size	1.85 mm
• Total 3D reconstructed image size	138 MB
• 2D image reconstruction time	40 secs.
• 3 D image reconstruction time	12 hours

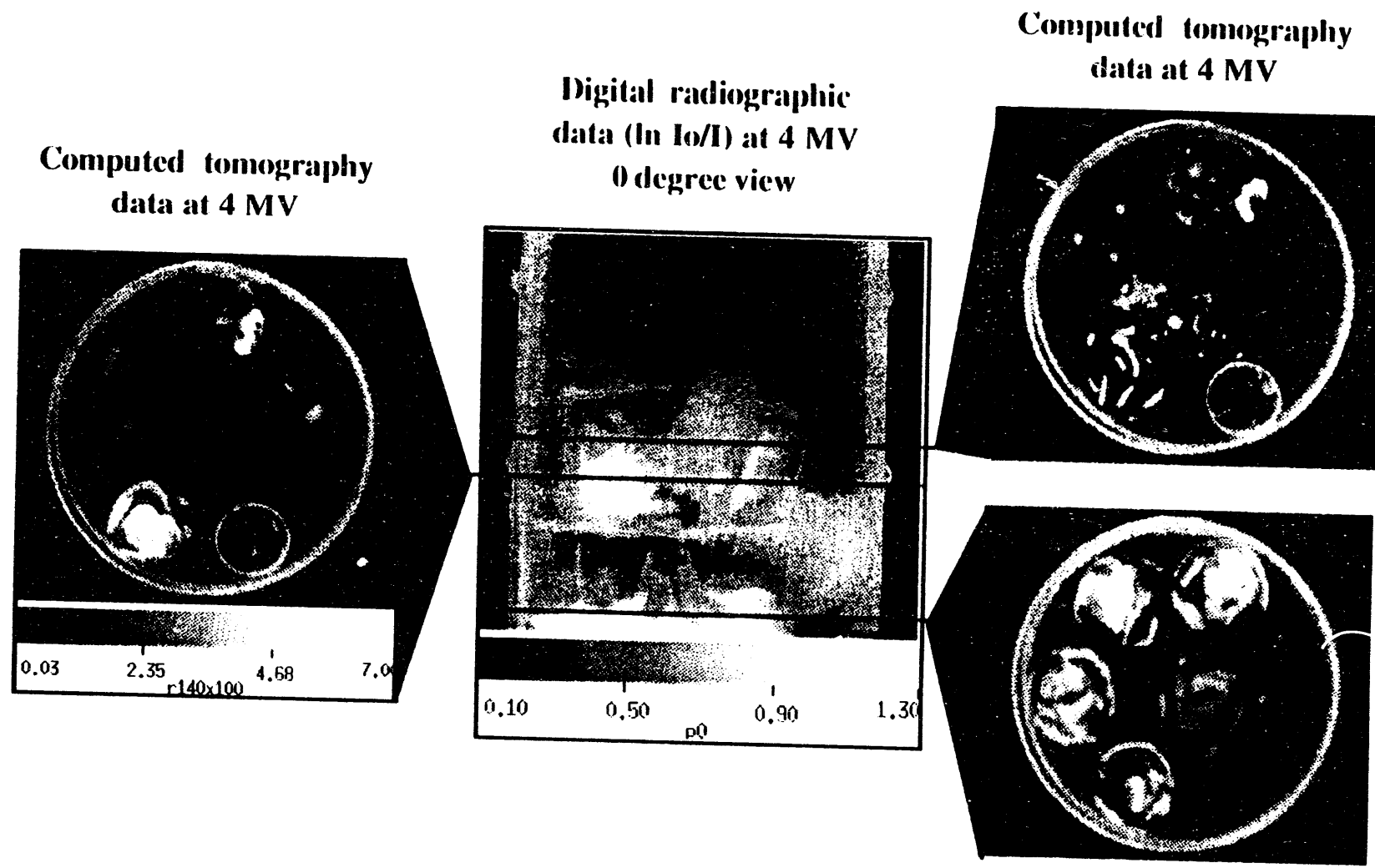
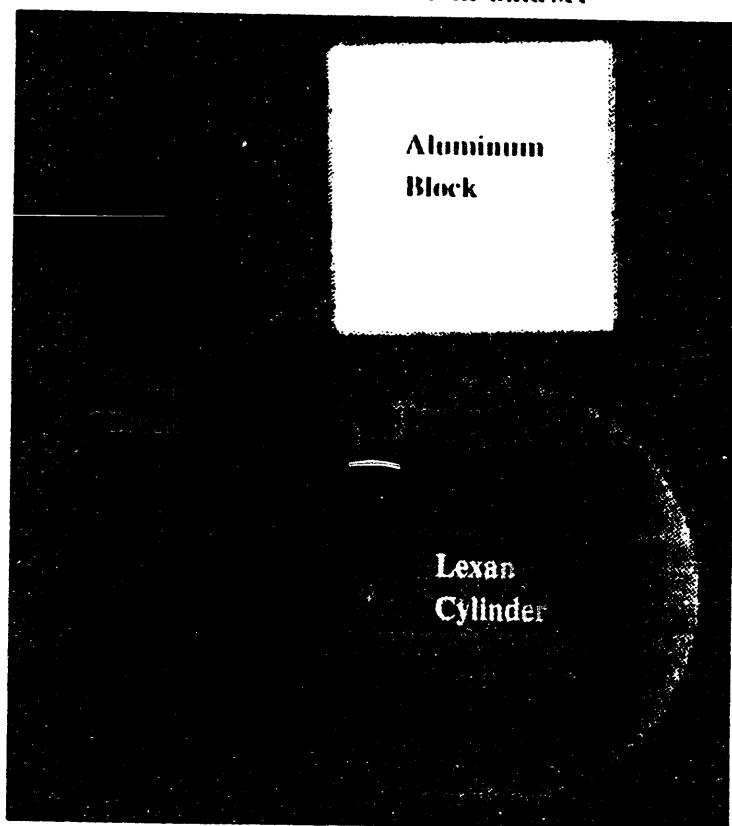


Figure 1: Representative 2D digital radiographic (center) and 2D-cross-sectional (sides) TCT images of a real transuranic waste drum. Note how the external and internal details are more easily revealed in the tomographic data as compared to the radiographic data. The gray scale relates tones in the DR image to $\ln I_0/I$. The gray scale under the tomographic image relates tones to relative attenuation.

For a magnification of 1.15, the detector dimensions at the object is 0.392 x 0.522 mm

Material	Total pixels	Measured volume	Calculated volume	Error
Wood	582792	46747 mm ³	32262 mm ³	30%
Lexan	750421	60193 mm ³	57916 mm ³	3.8%
Aluminum	408544	32770 mm ³	32774 mm ³	0.01%

CT slice #47 of volume data set



Histogram of slice #47

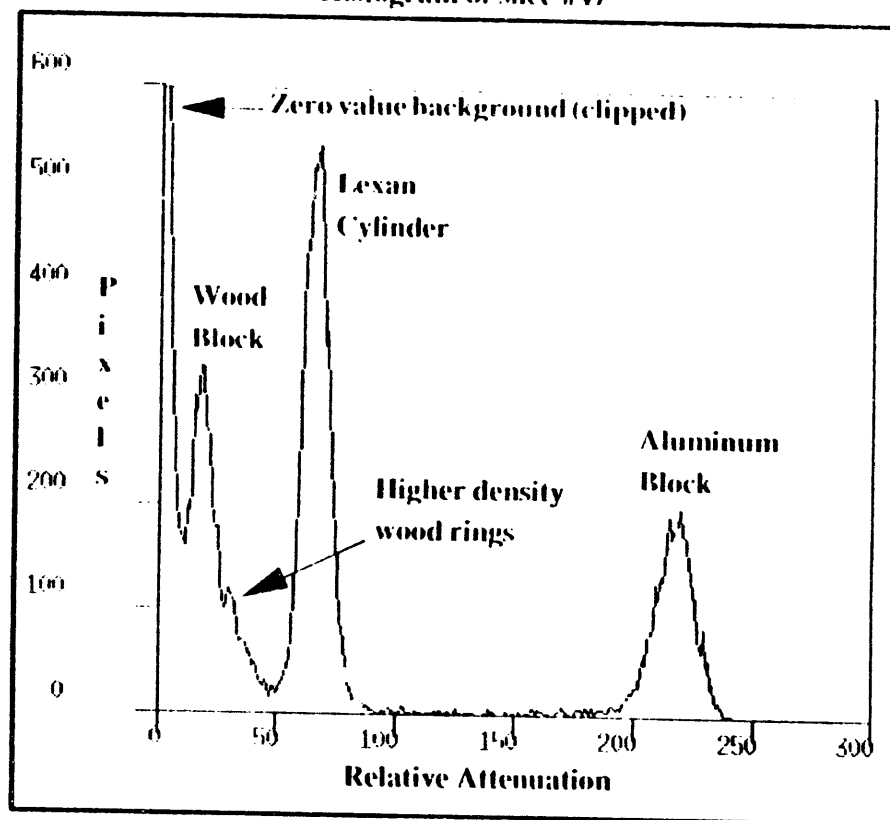


Figure 2: Representative example of how TCT data can be used to quantitatively determine volumes of different materials. At the top are the quantitative results for a TCT volume image. A representative tomogram of the TCT volume is shown to the bottom left. A histogram for this tomogram is shown to the bottom right.

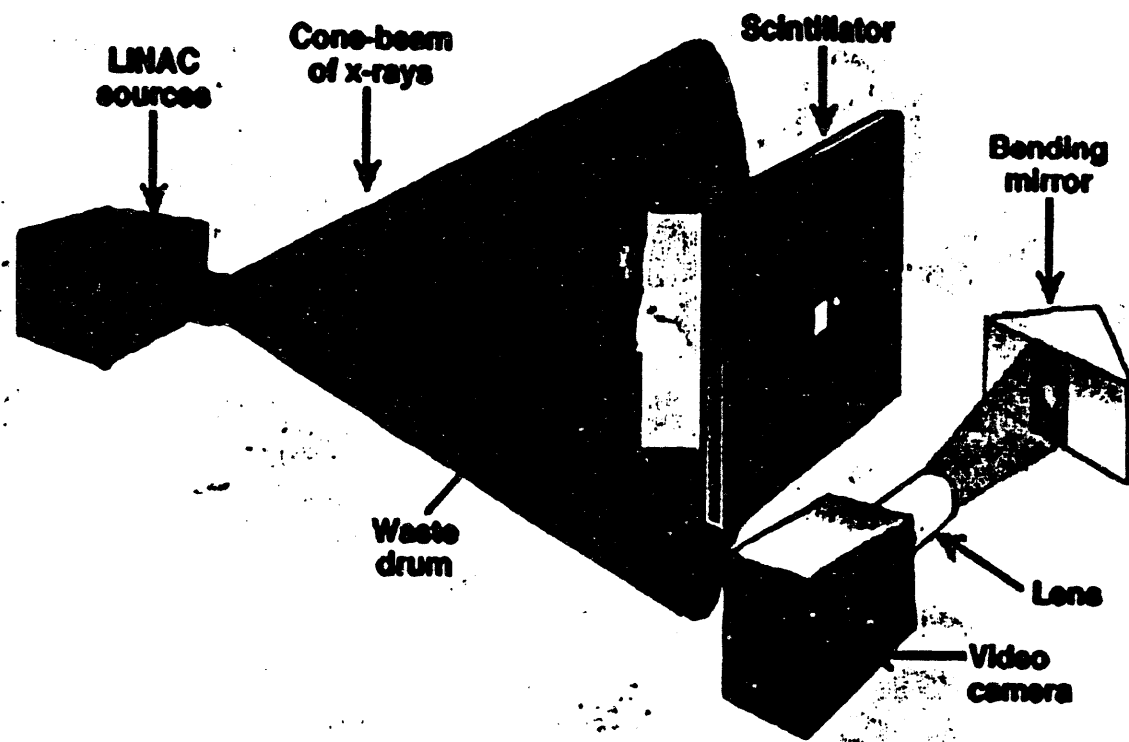


Figure 3: Artists conceptual drawing of typical LLNL system components for a 2D detector with no collimation on the detector side. These components can be used to obtain all three x-ray NDE (i.e., RTR, DR, and TCT) data sets.

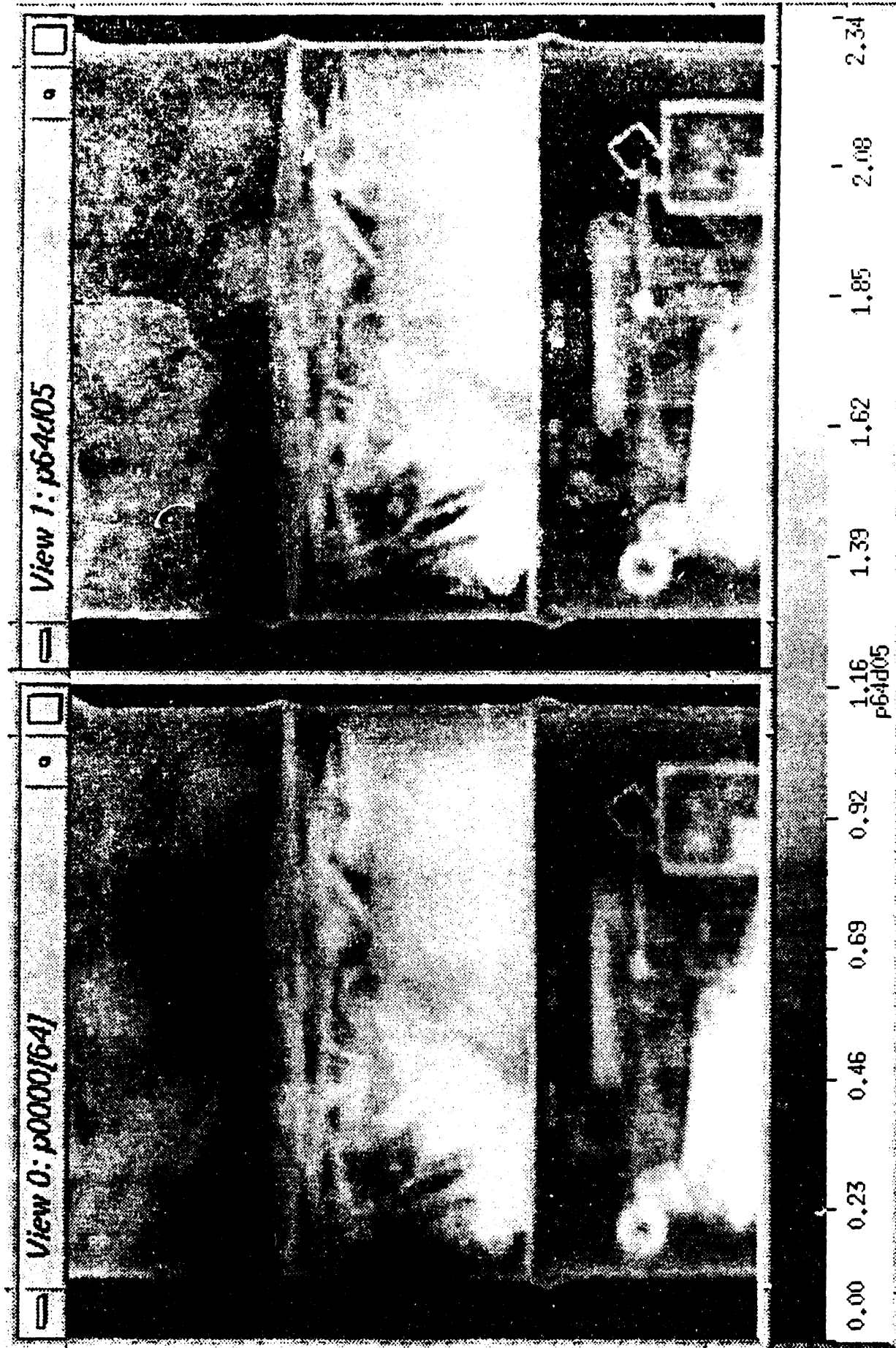


Figure 4: Representative radiographic images before (left) and after (right) deconvolution by a Lorentzian shaped point spread function.

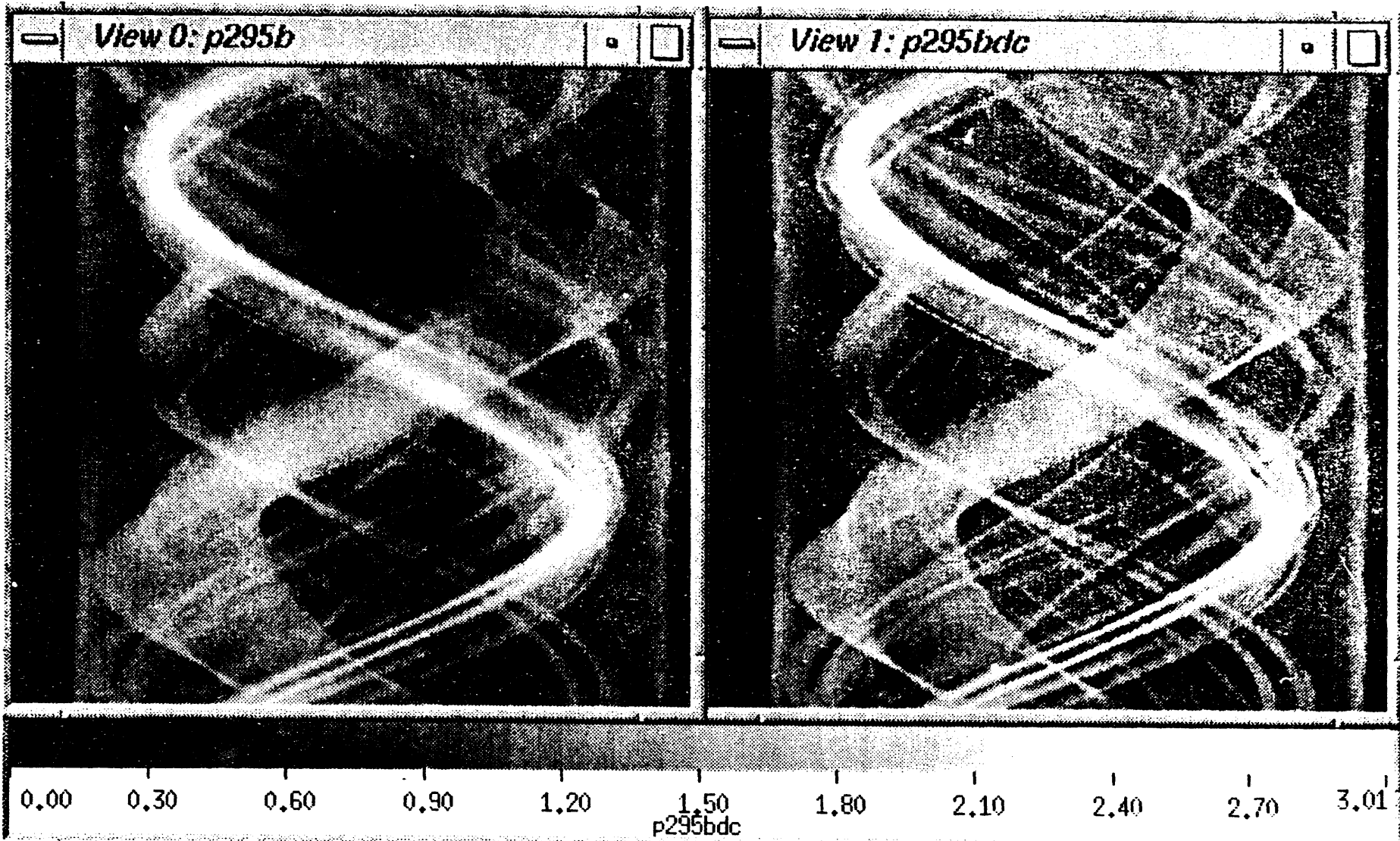


Figure 5: Representative sinogram images before (left) and after (right) deconvolution by a Lorentzian shaped point spread function.

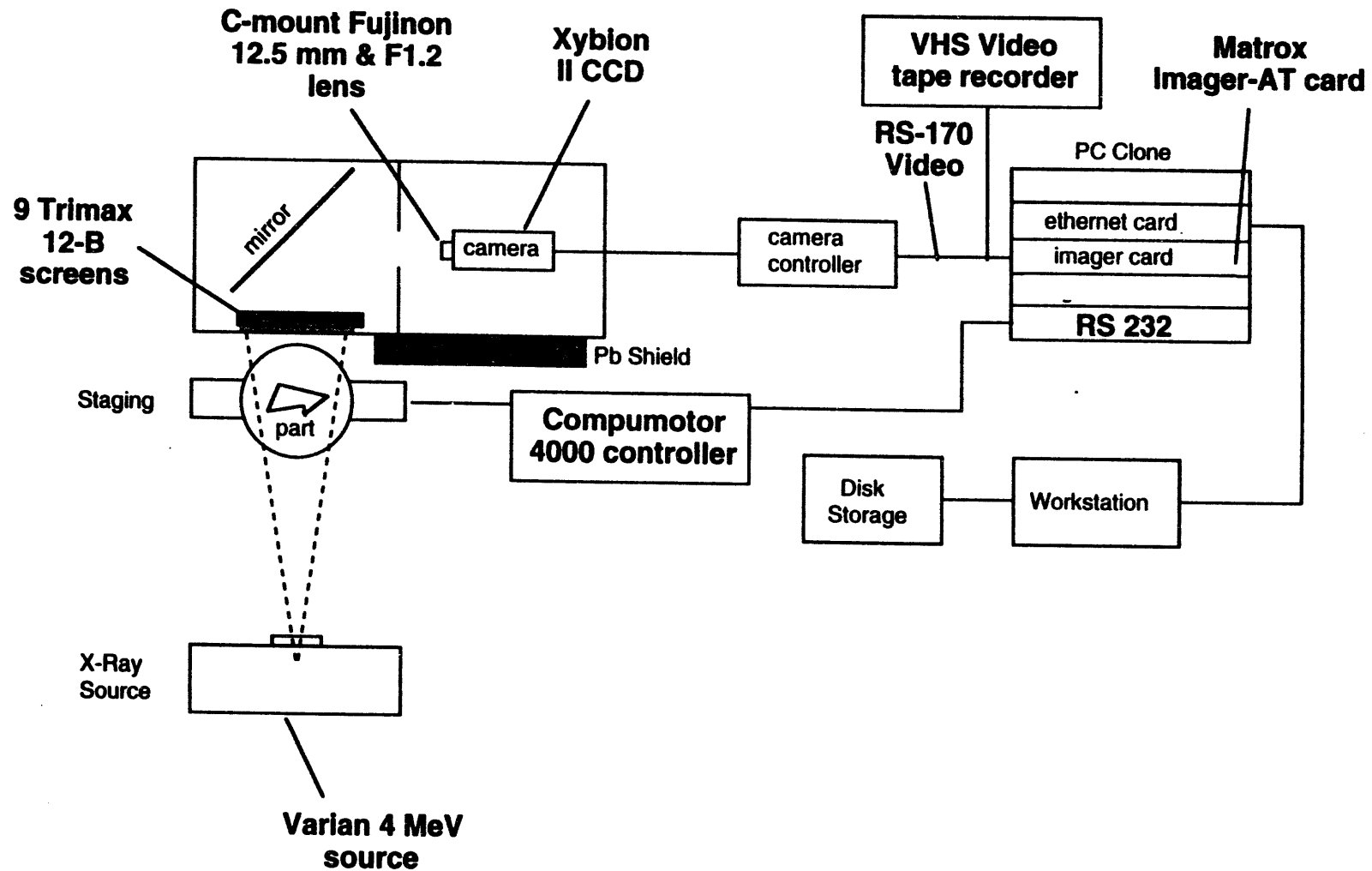


Figure 6: Schematic diagram of an inexpensive x-ray NDE waste drum characterization system developed at LLNL. Most of the important system components are labeled in the diagram.

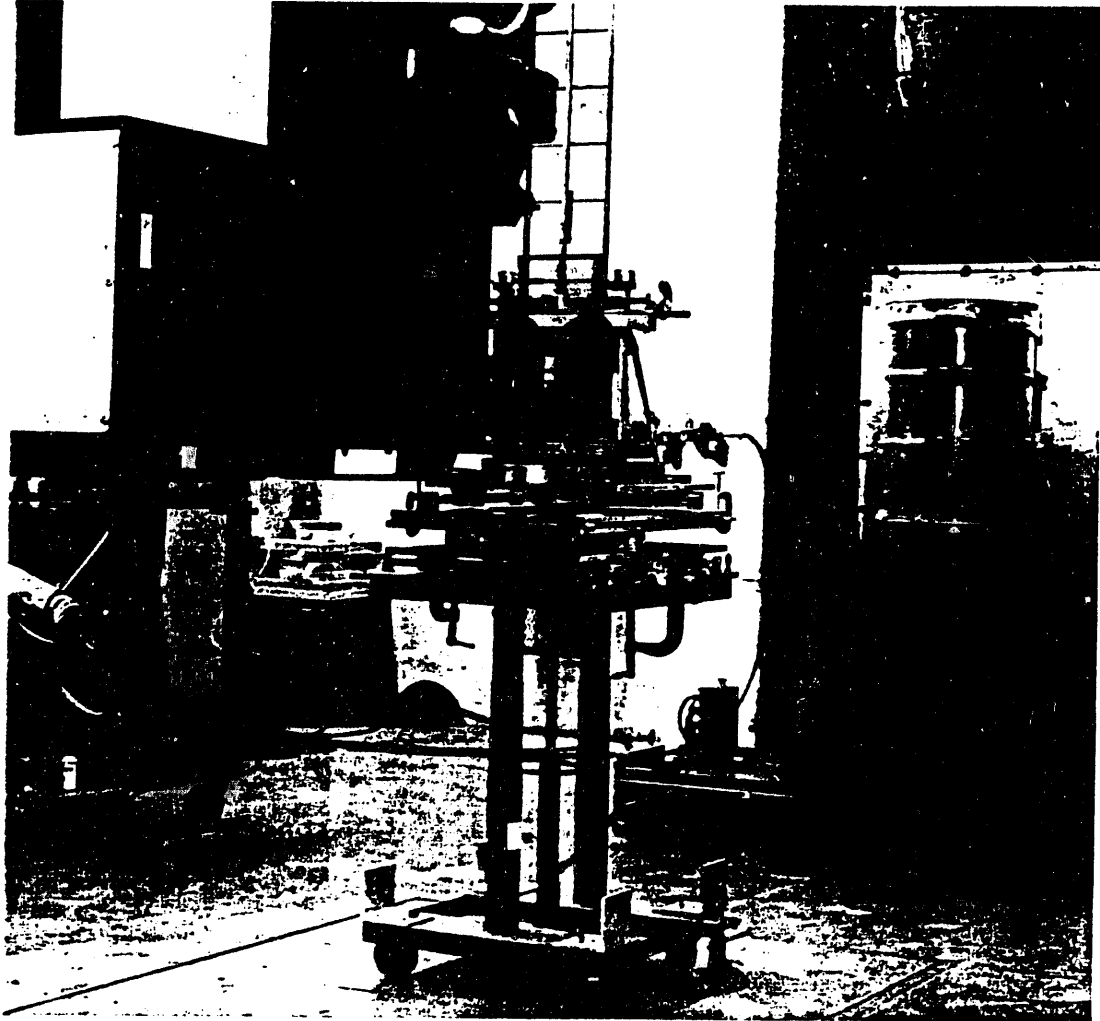


Figure 7: Photograph of the NDE waste drum characterization system. From left to right are the 4-MeV LINAC x-ray source, secondary collimation, waste drum/drum manipulator, and 2D or area-array detector. The detector is a large area-array imager. Further details of the detector are shown in Figures 3 and 6.

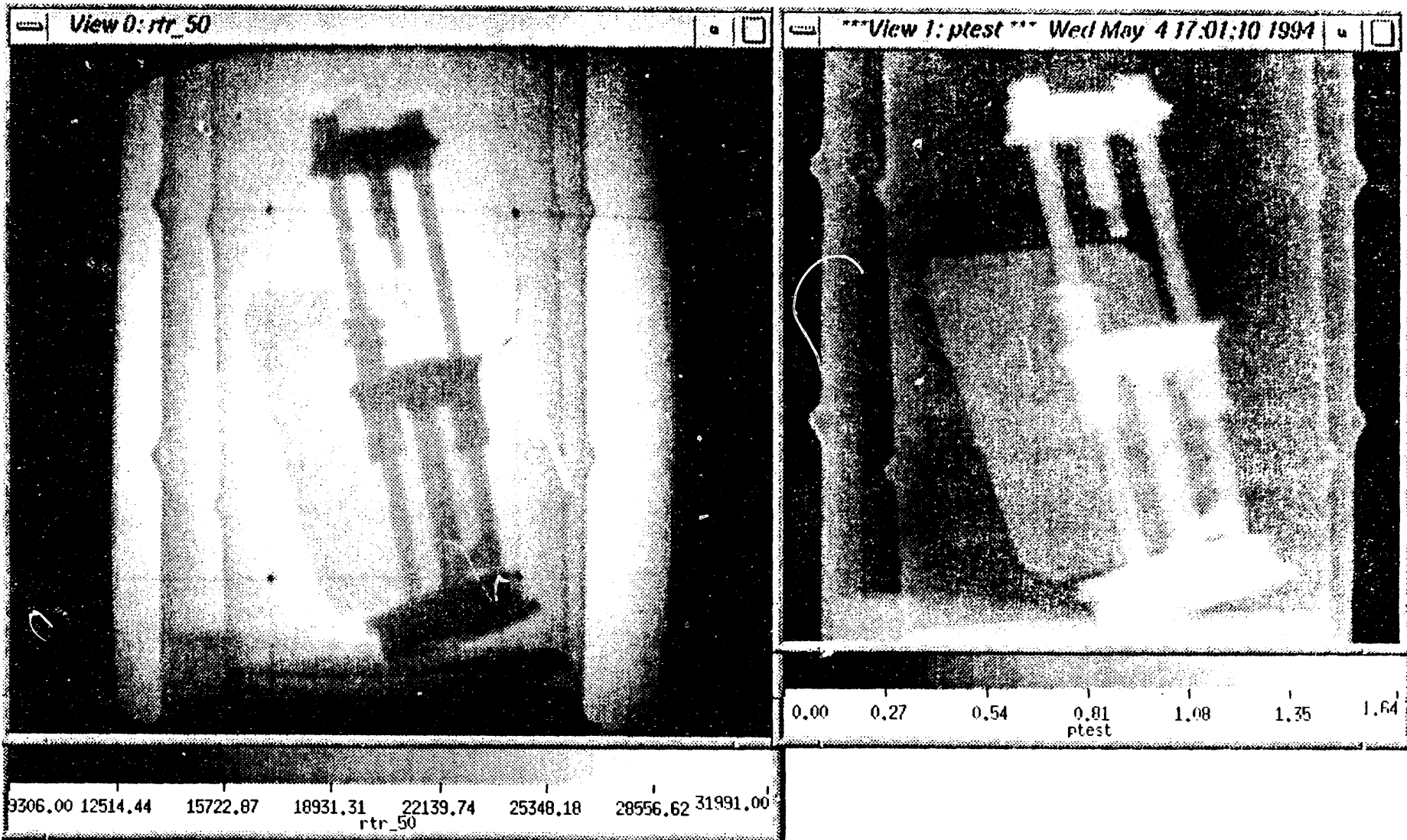


Figure 8: Representative intensity (left) and corrected (right)—see text for corrections applied— digital radiographic images for a TRU waste drum. The gray scale on the left relates tones in the image to intensity, on the right it relates tones to $\ln I_0/I$.

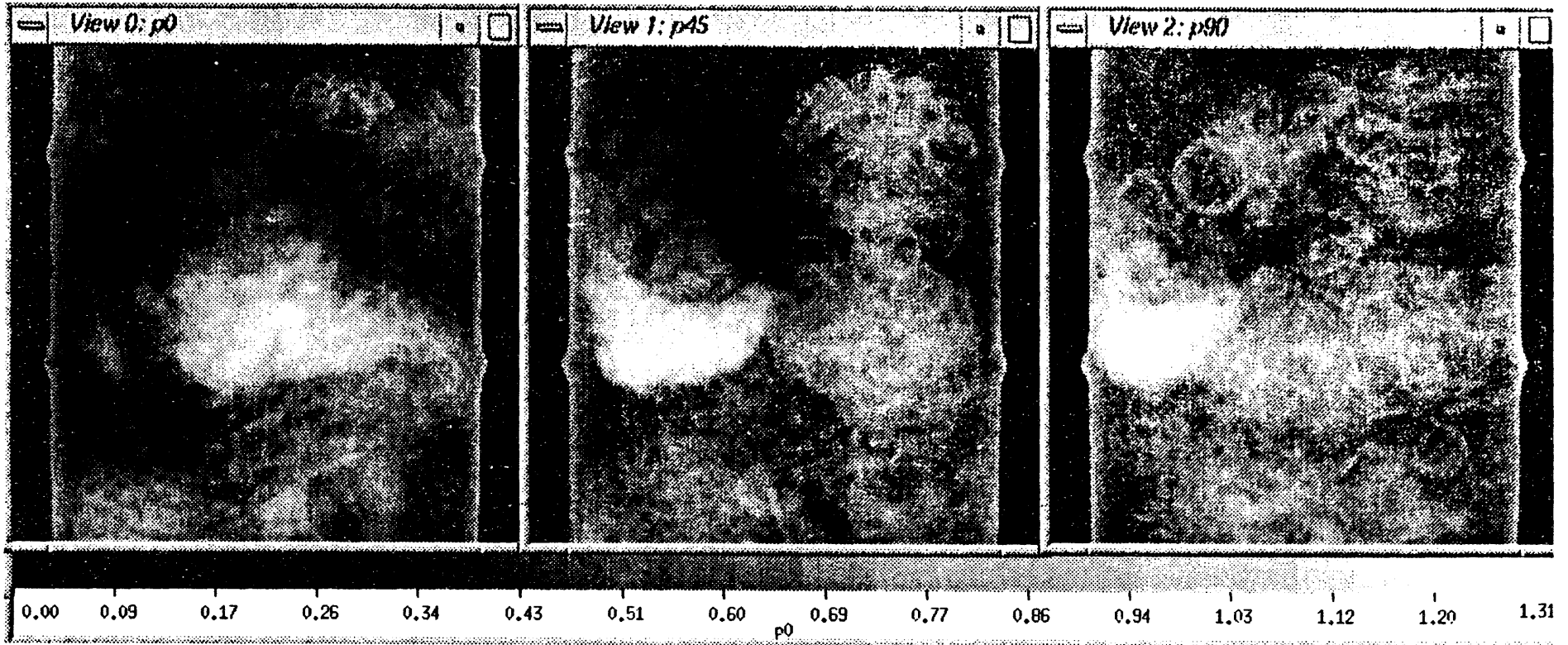


Figure 9: Representative digital radiographic images for a real LLW drum with a glass matrix. From left to right are views at 0°, 45°, and 90°, respectively. The gray scale relates tones in the image to $\ln I_0/I$.

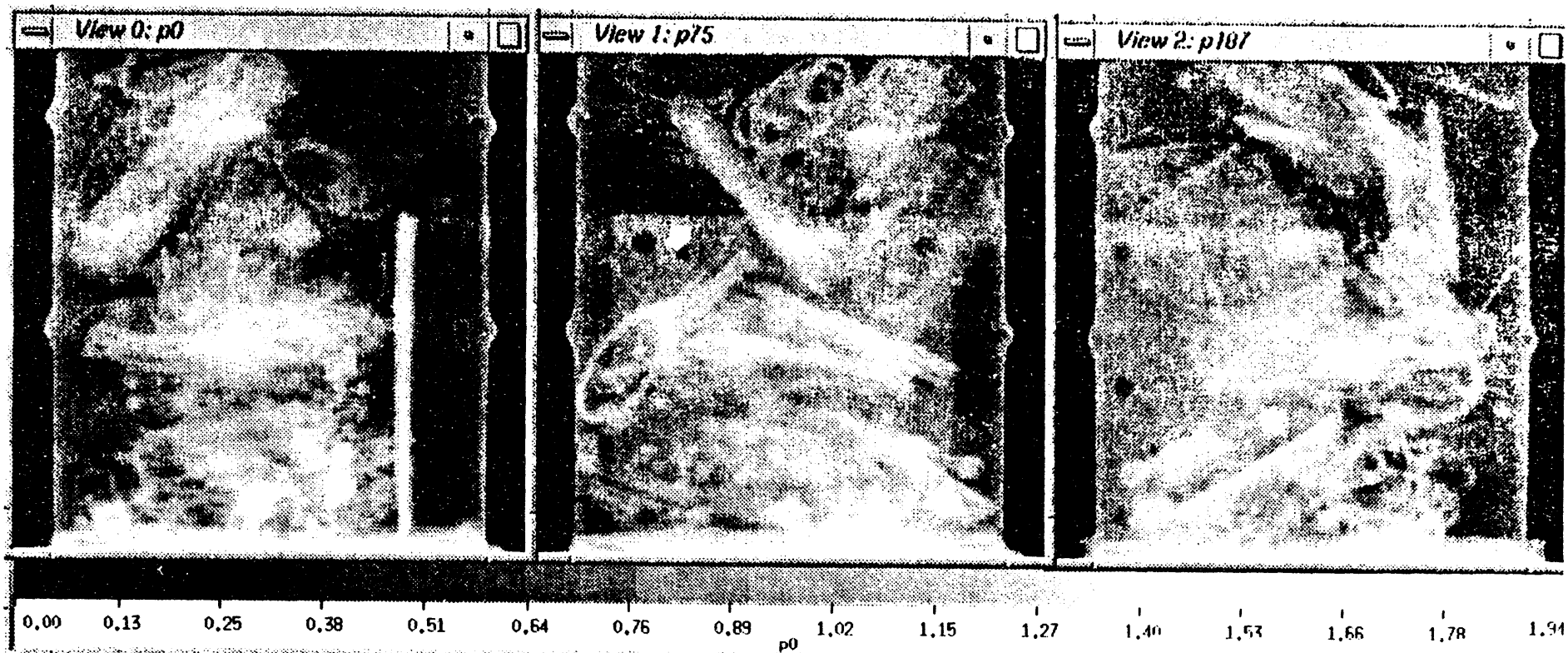


Figure 10: Representative digital radiographic images for a real LLW drum with a metal matrix. From left to right are views at 0°, 90°, and 225°, respectively. The gray scale relates tones in the image to $\ln I_0/I$.

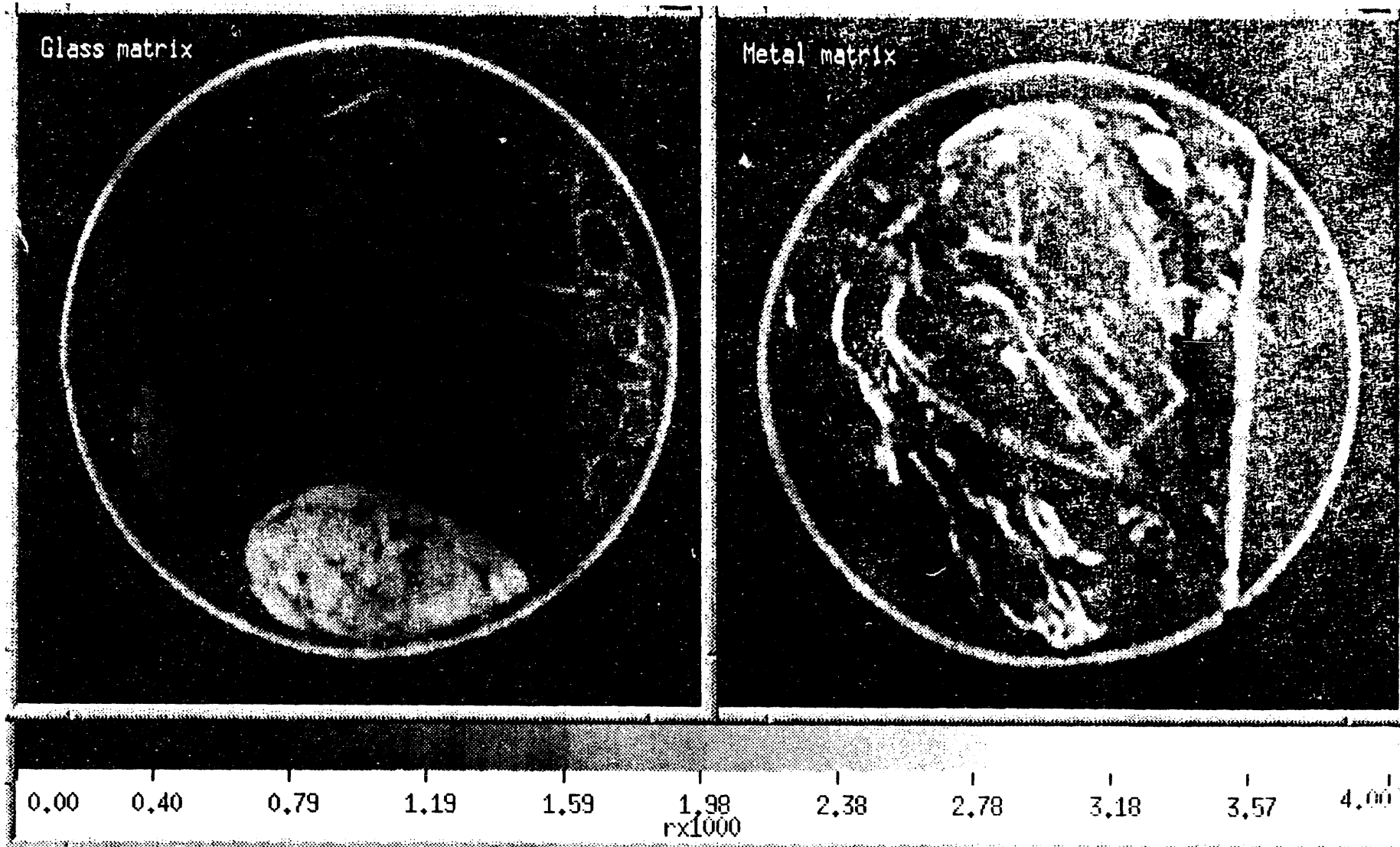


Figure 11: Representative transmission CT images for the LLW drums with glass (left) and metal (right) matrices. The gray scale relates relative attenuation values to tones in each image. Their

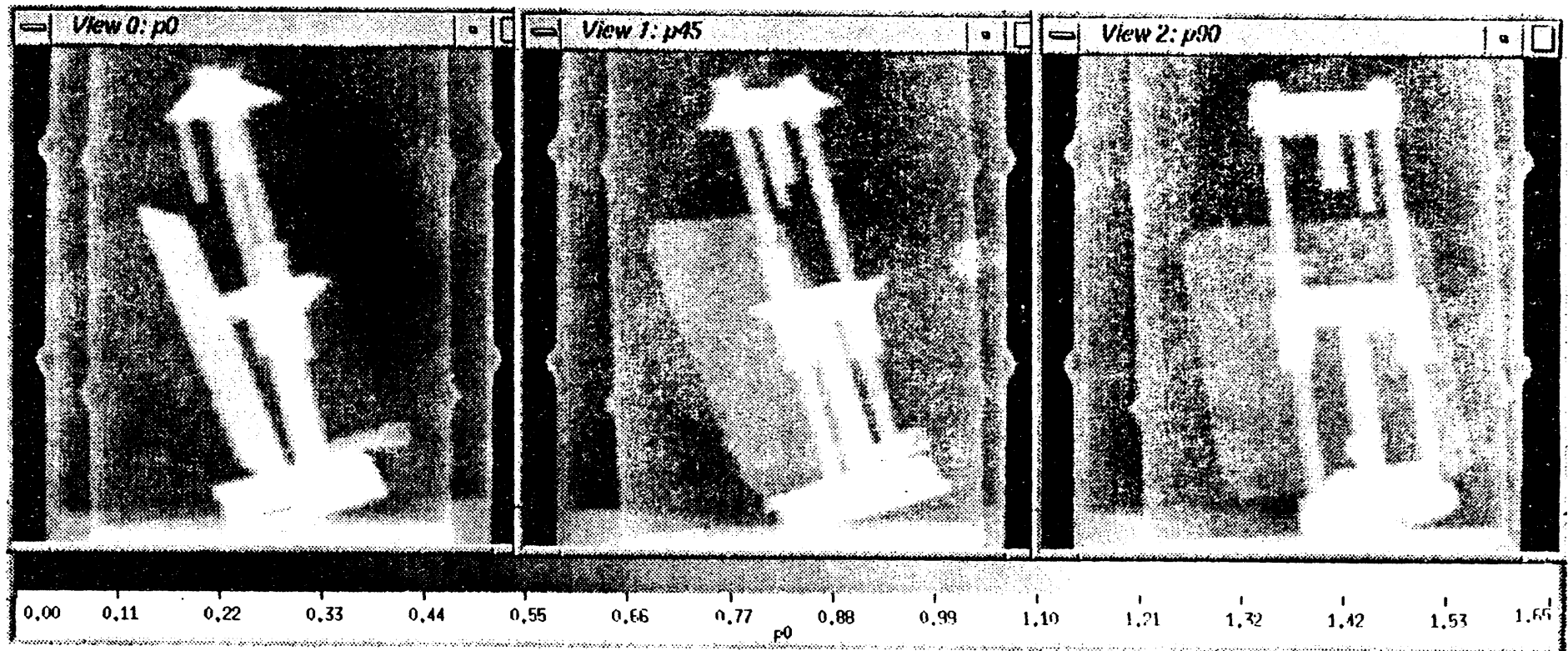


Figure 12: Representative digital radiographic images for a real TRU-waste drum that contains a hydraulic jack within another container. From left to right are views at 0°, 45°, and 90°, respectively. The gray scale relates tones in the image to $\ln I_0/I$.

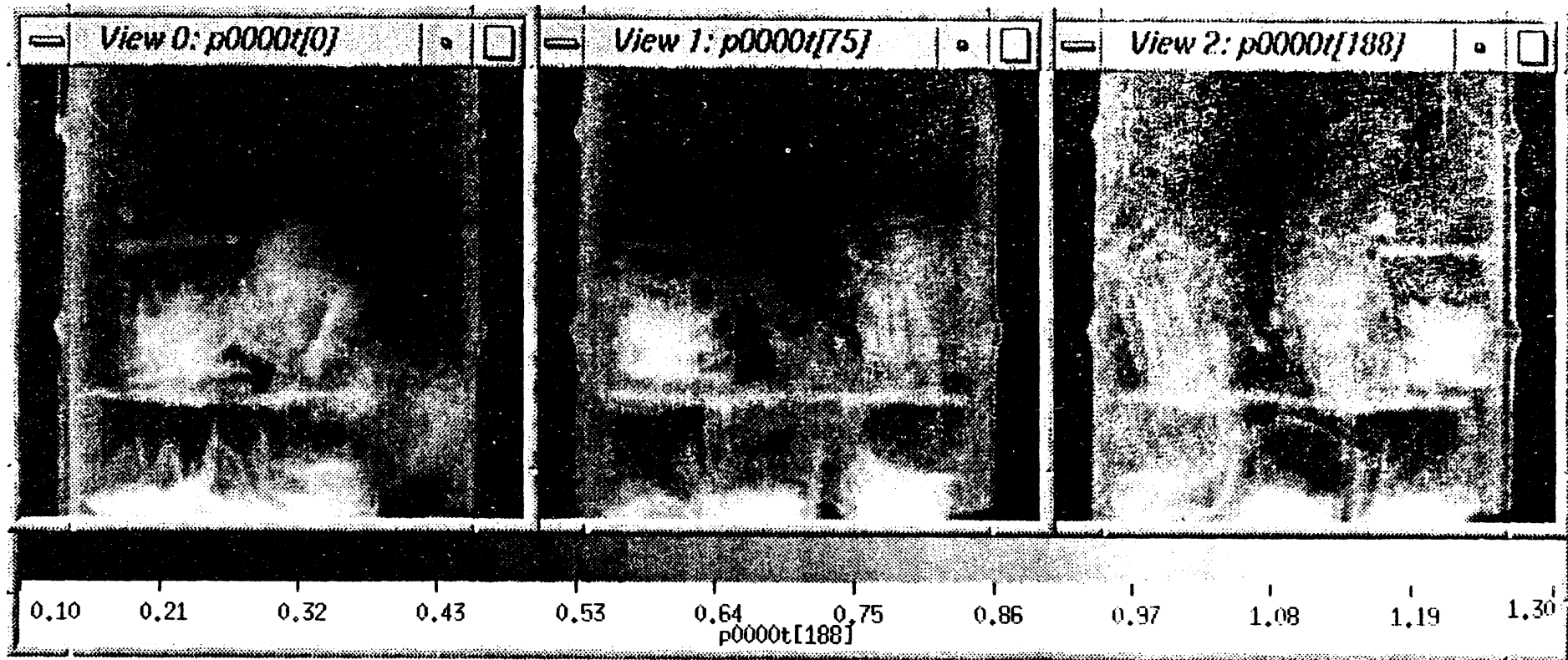


Figure 13: Representative digital radiographic images for a TRU waste drum that contains broken ceramic crucibles contaminated with Pu among other waste items. From left to right are views at 0°, 90°, and 225°, respectively. The gray scale relates tones in the image to $\ln I_0/I$.

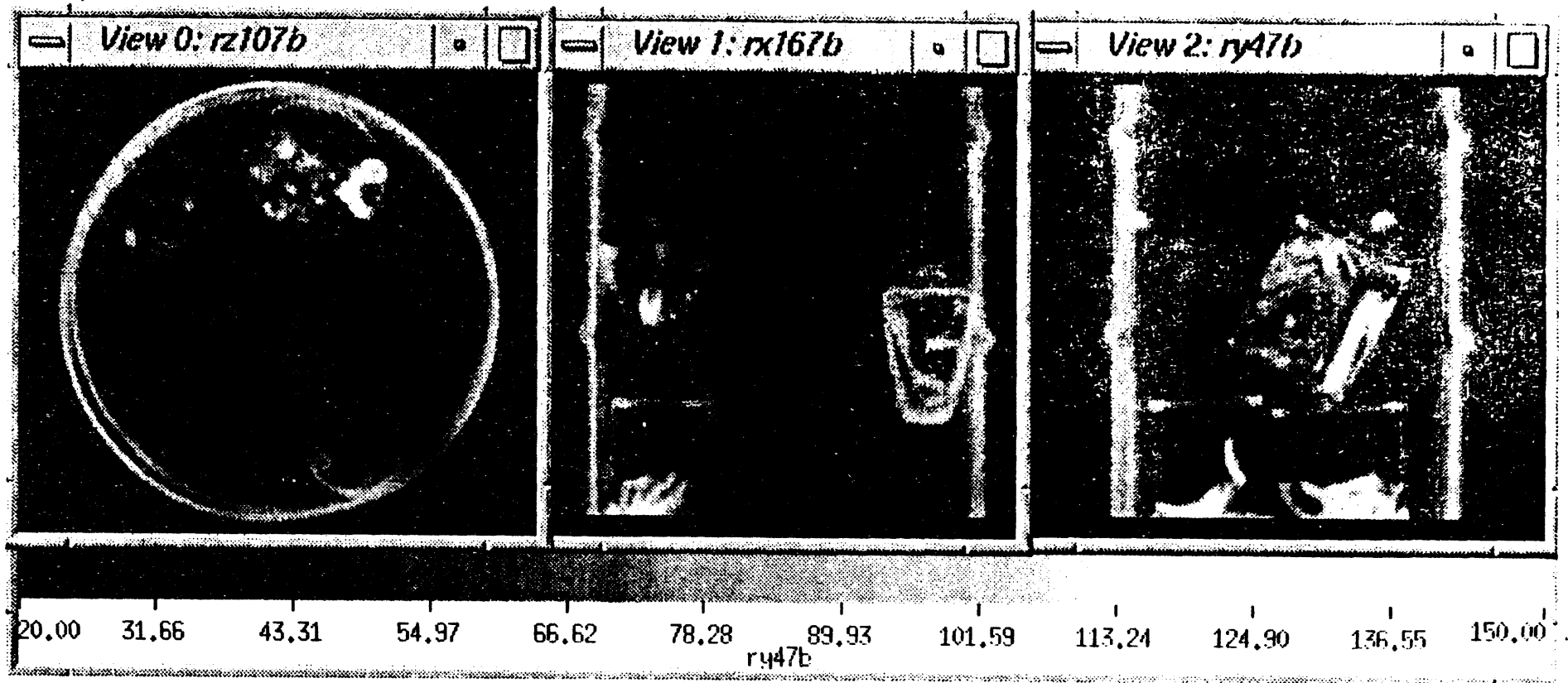


Figure 14: Representative transmission CT images for the TRU drum that contains broken crucibles contaminated with Pu. Three images are shown that reveal the true 3D nature of TCT. These images represent cross-sectional views computationally extracted along the z-, x- and y-axis, respectively of a volumetric image. The gray scale relates tones in the image to relative attenuation.

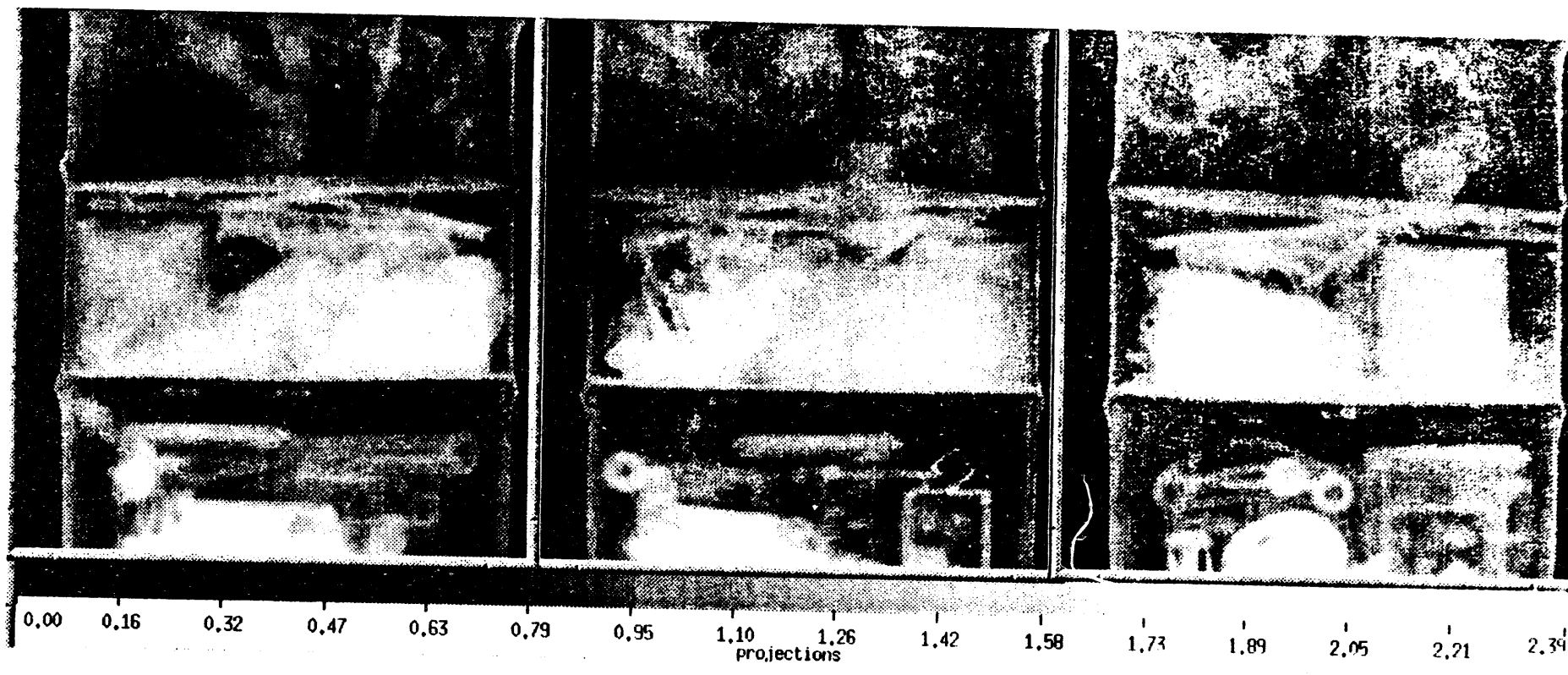


Figure 15: Representative digital radiographic images for one of the mock-waste drums to be used in the performance analysis of the A&PCT scanner. The radiographs are at different angles to show various aspects of the contents of the waste drum. The gray scale relates tones in the image to $\ln I_0/I$.

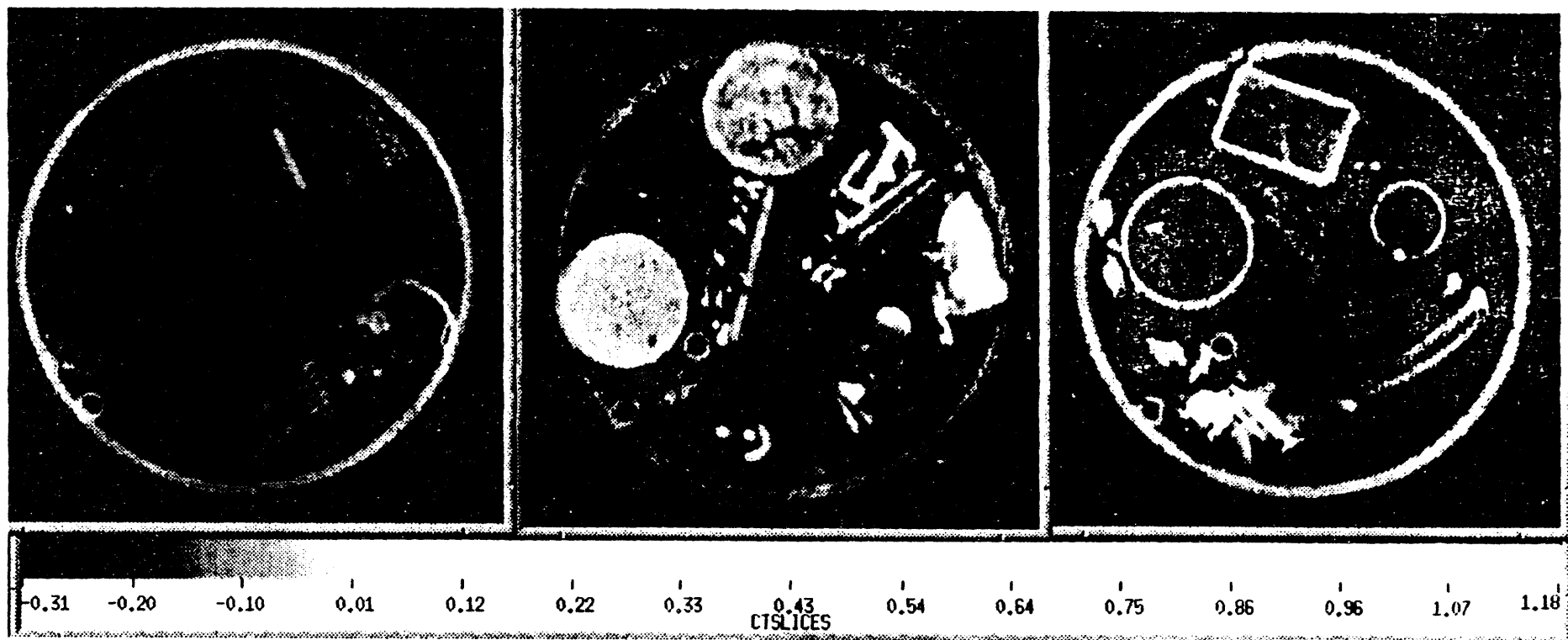


Figure 16: Representative transmission CT images for the mock drum shown in Figure 15. From left to right are cross-sectional views of the low- and medium-density LLW sections and the TRU-waste section, respectively.

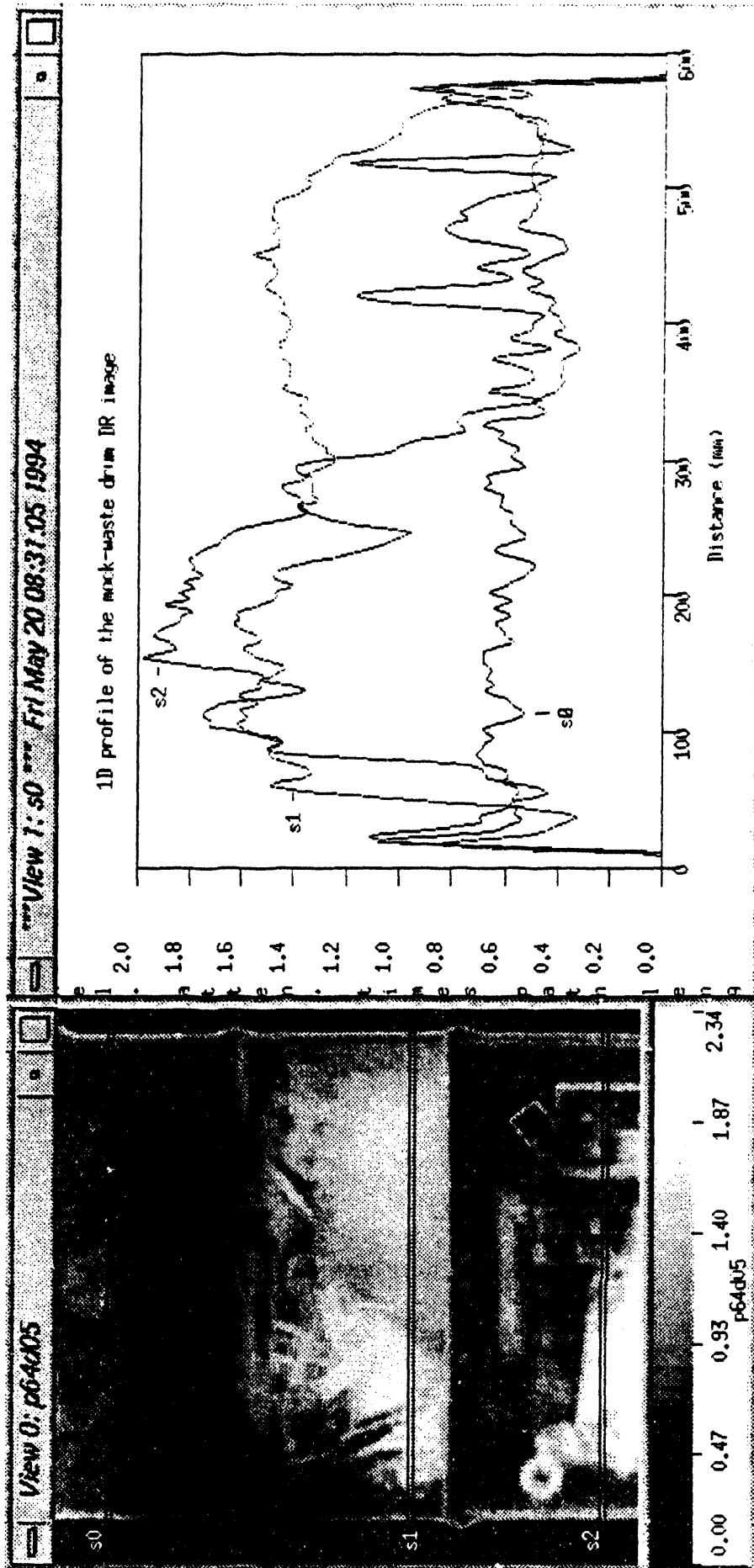


Figure 17: Digital radiographic image of the mock-waste drum with 1D profiles extracted and plotted to the right as labeled.

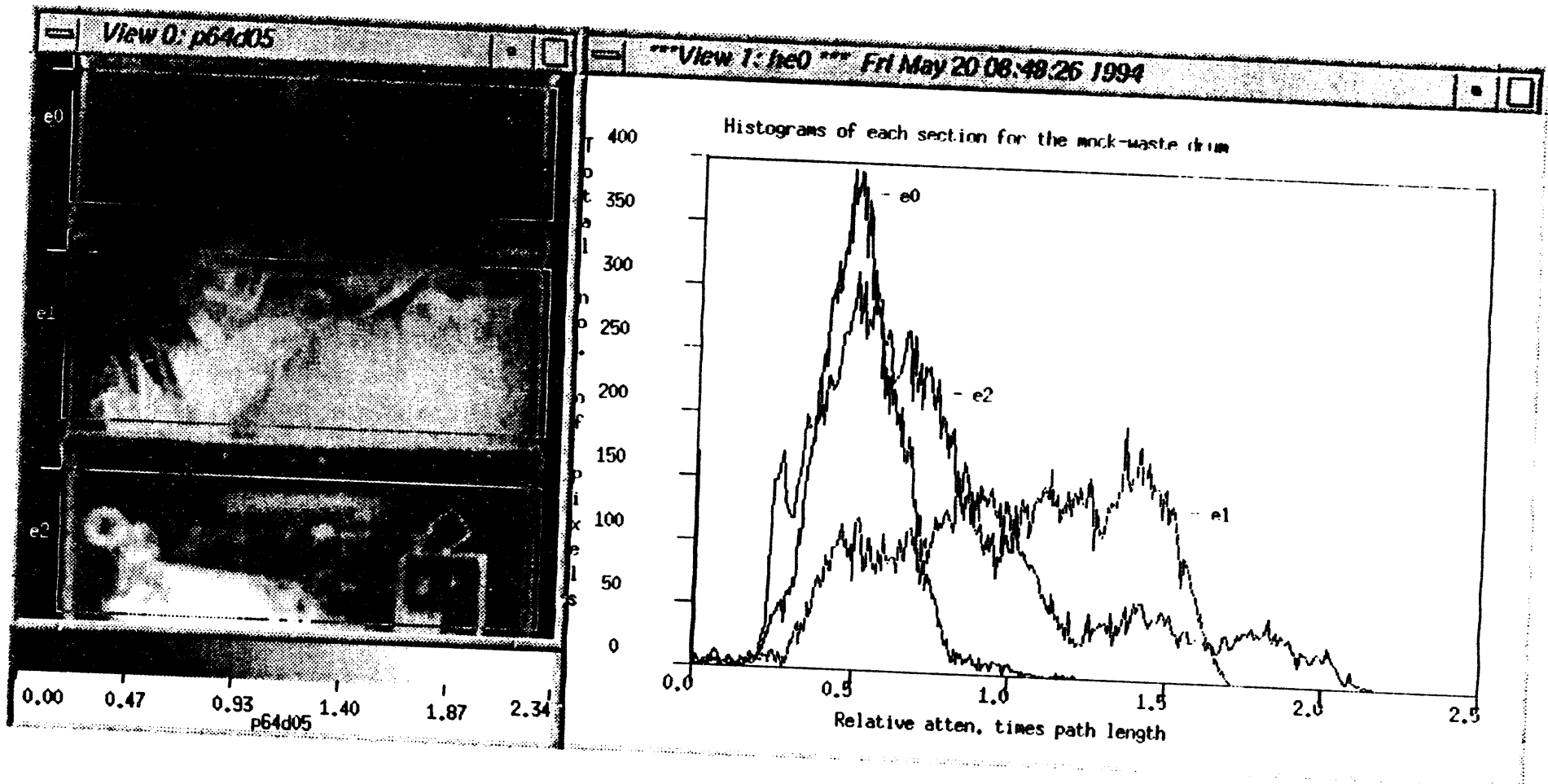


Figure 18: Histograms were determined for the extracted areas as shown in the DR image and are plotted to the right as labeled.

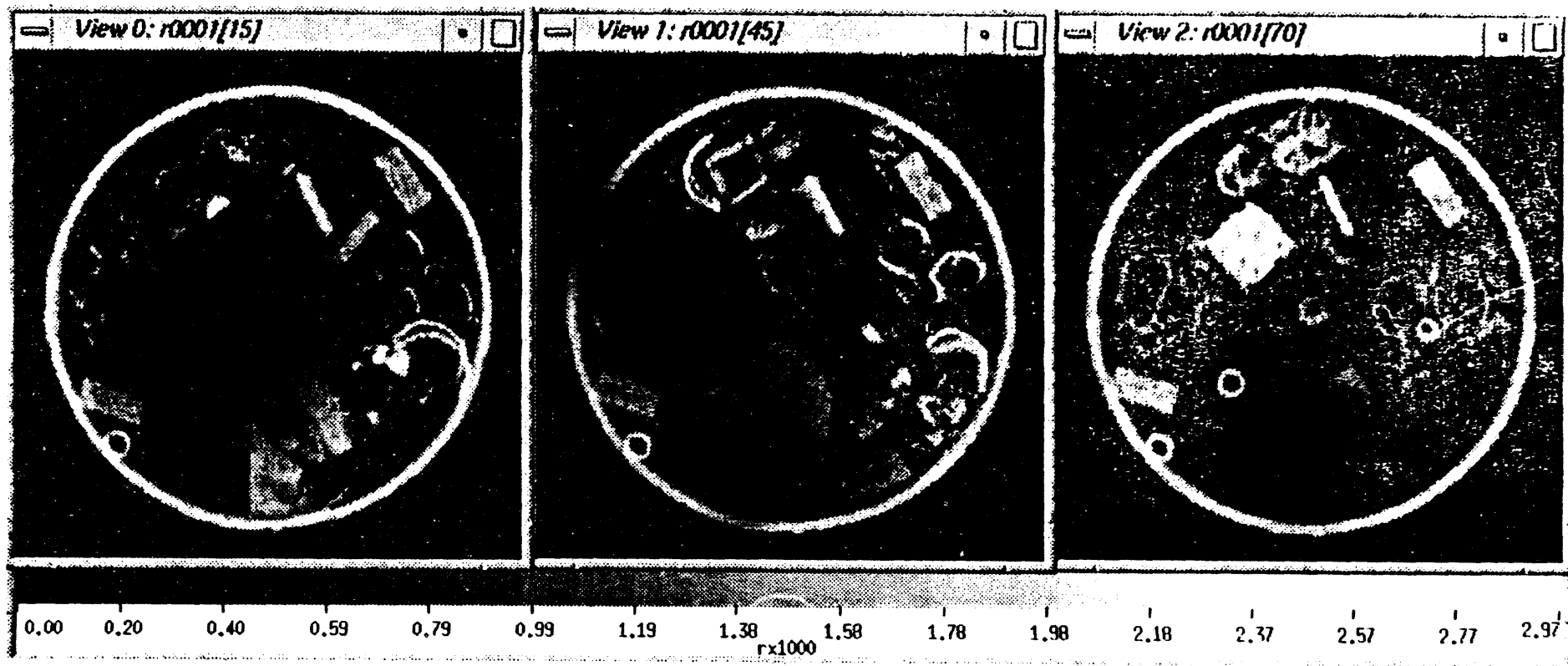


Figure 19: Three representative tomograms that reveal several items contained in the top or low-density LLW matrix portion of the mock drum.

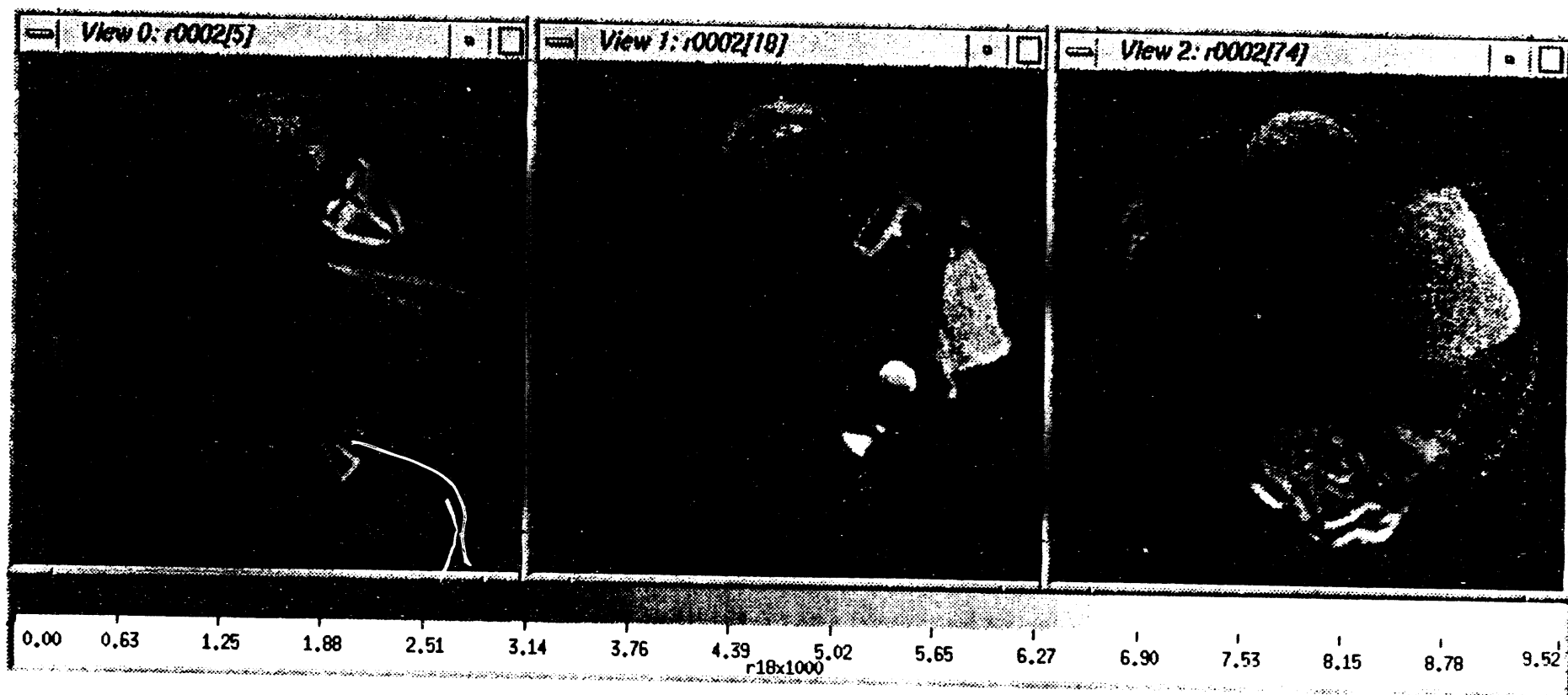


Figure 20: Three representative tomograms that reveal several items contained in the middle or medium-density L.I.W matrix portion of the mock drum.

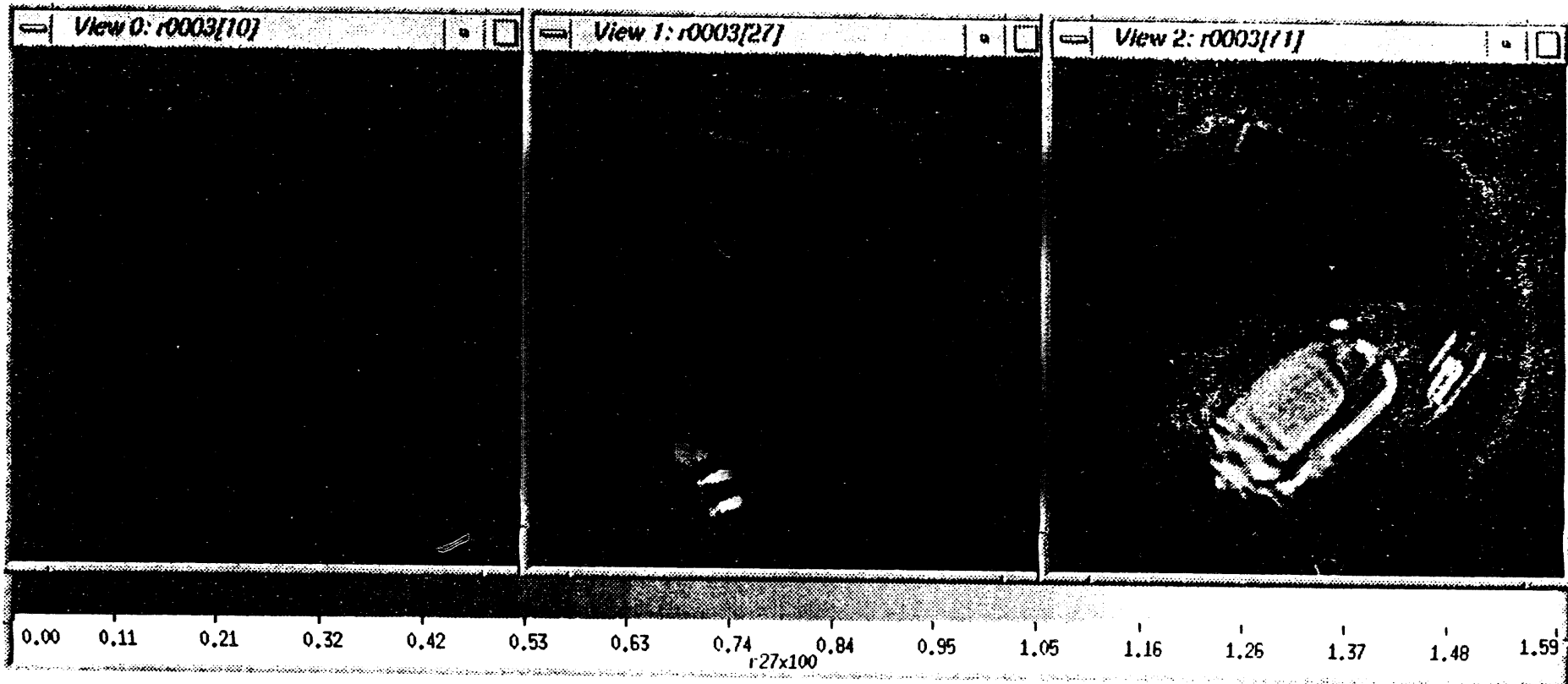


Figure 21: Three representative tomograms that reveal several items contained in the bottom or medium-density LLW matrix portion of the TRU-waste drum.

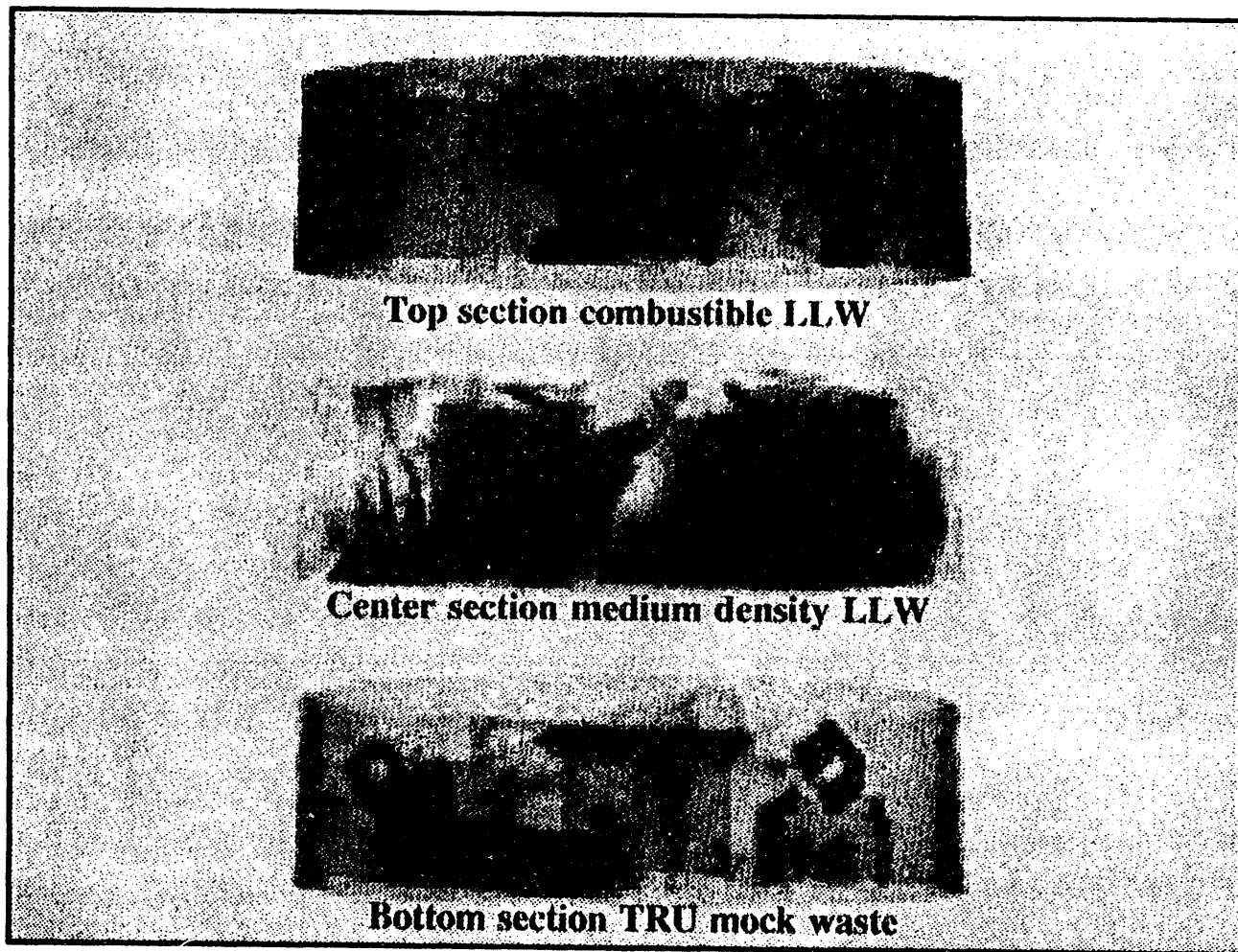


Figure 22: 3D volume rendered images from individual 2D tomographic images for all three waste matrices contained within the mock-waste drum.

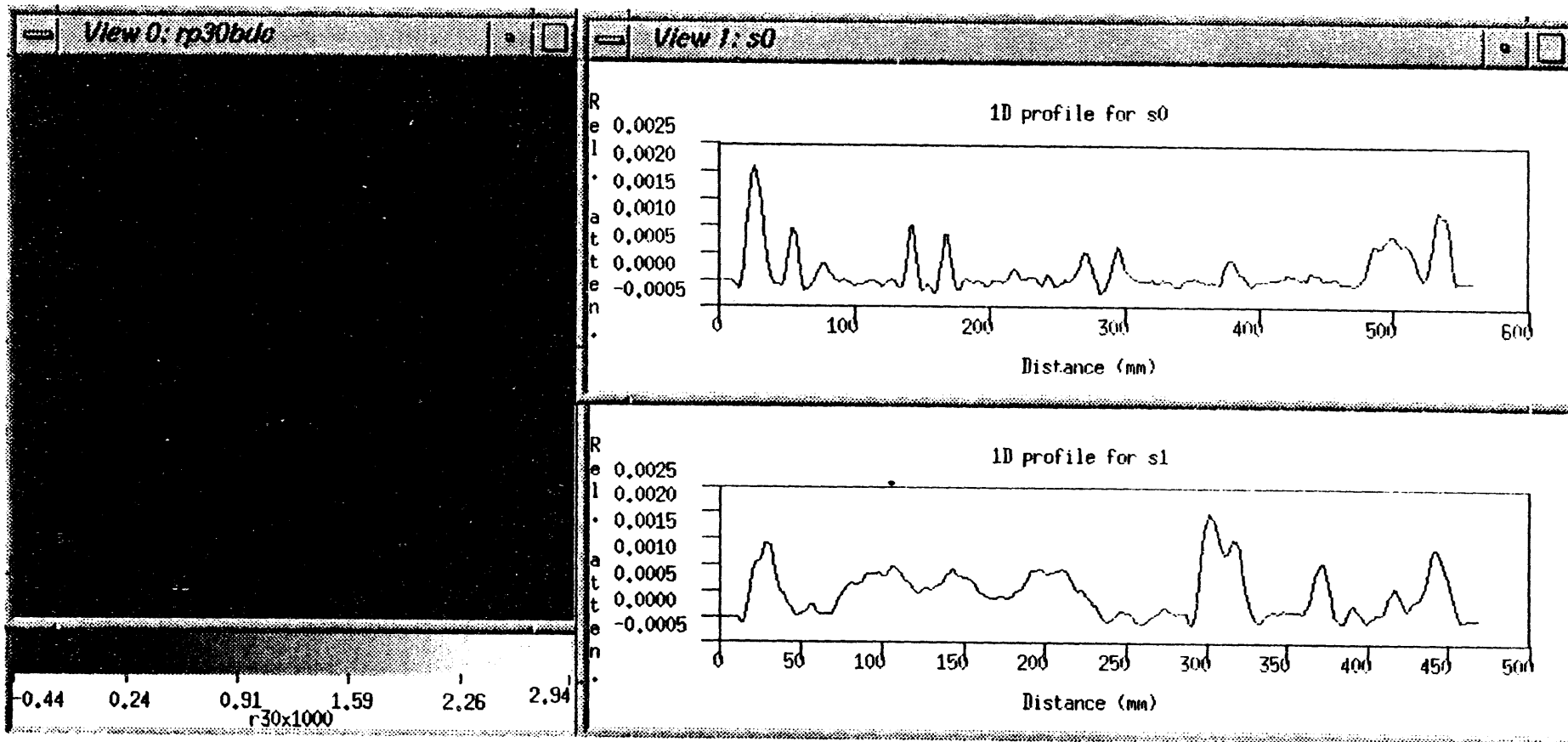


Figure 23: Representative CT image for the low-density LLW matrix with 1D profiles extracted and plotted to the right as labeled.

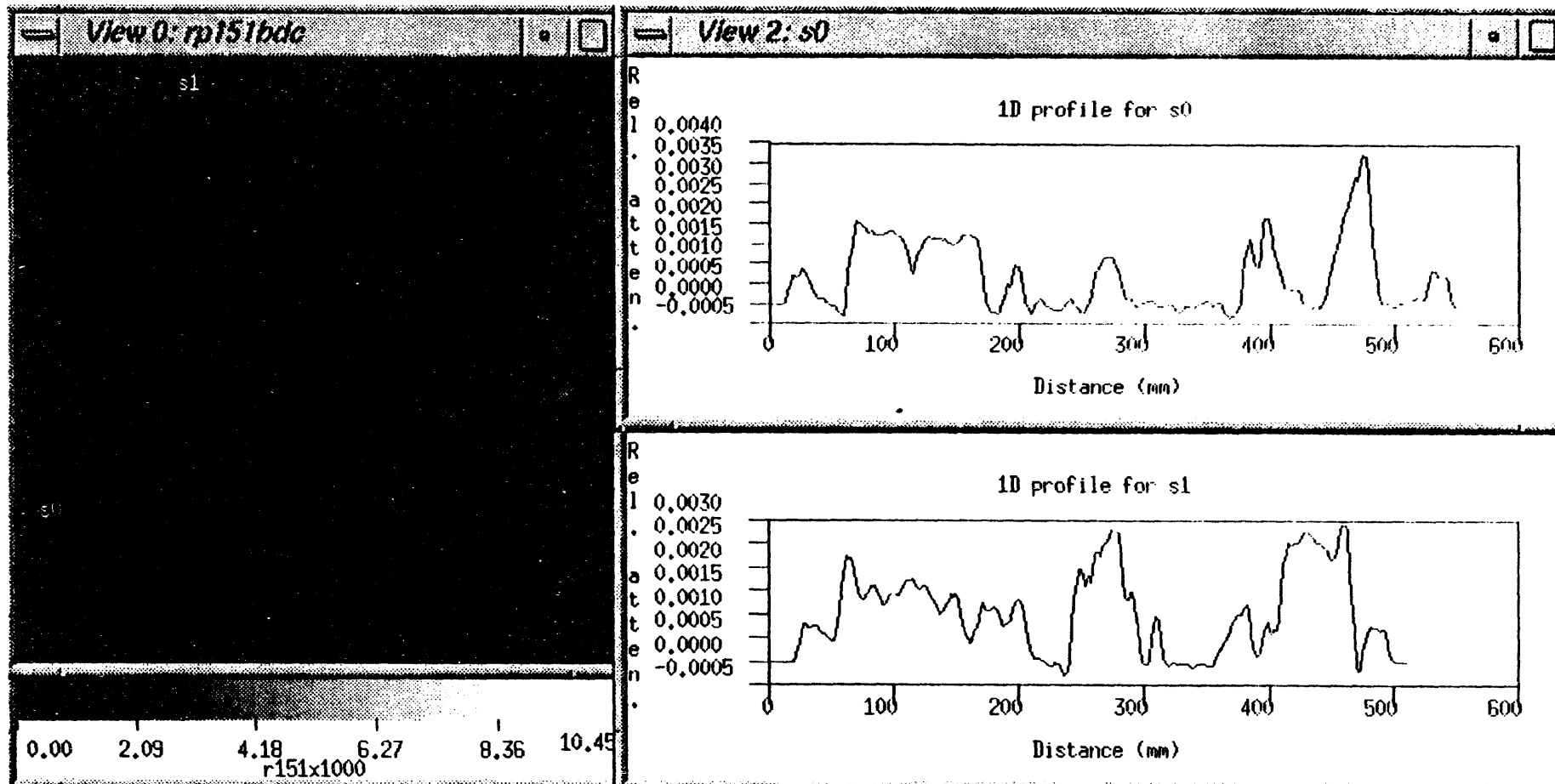


Figure 24: Representative CT image for the medium-density LLW matrix with 1D profiles extracted and plotted to the right as labeled.

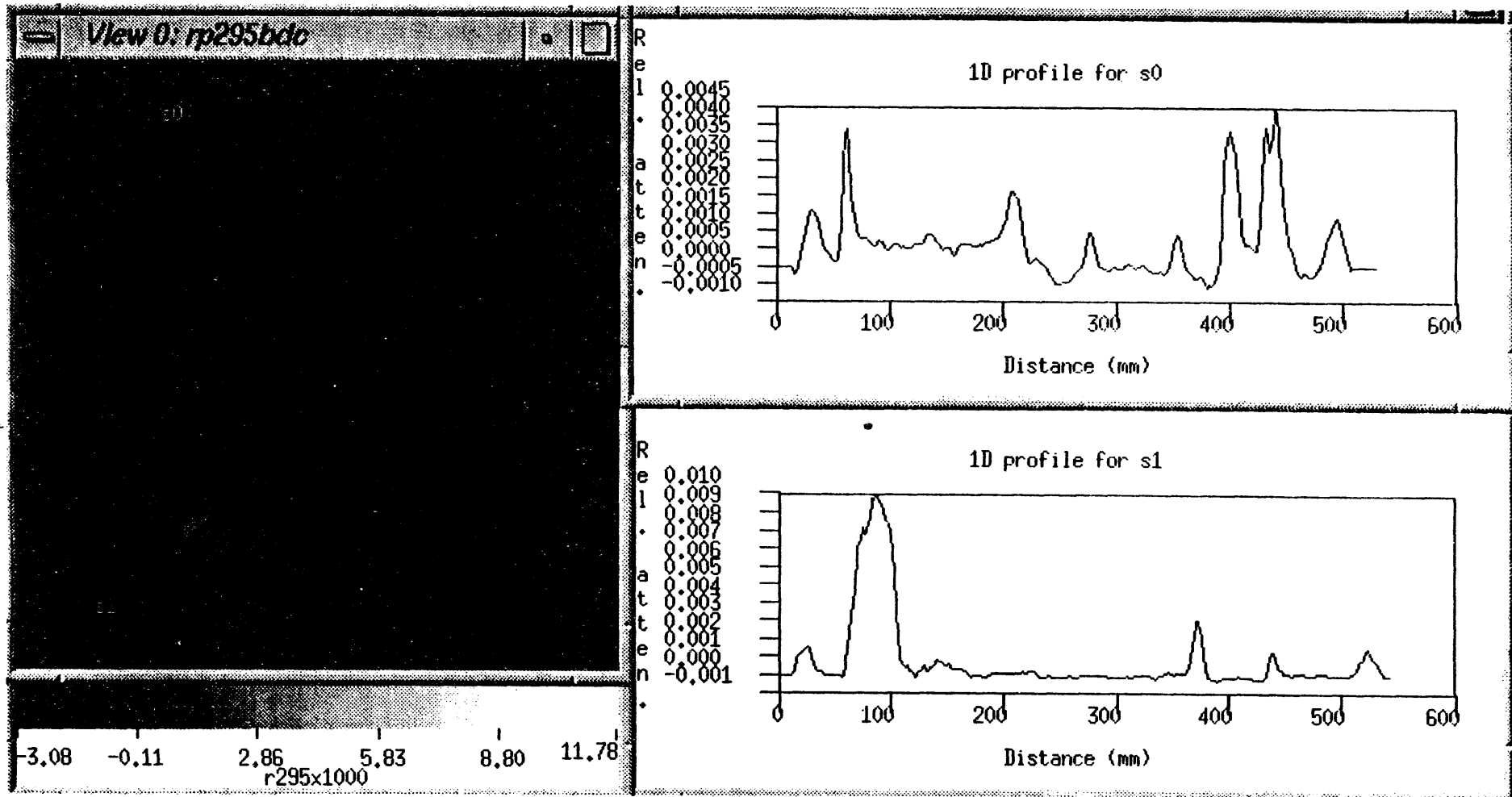


Figure 25: Representative CT image for the medium-density TRU-waste matrix with 1D profiles extracted and plotted to the right as labeled.

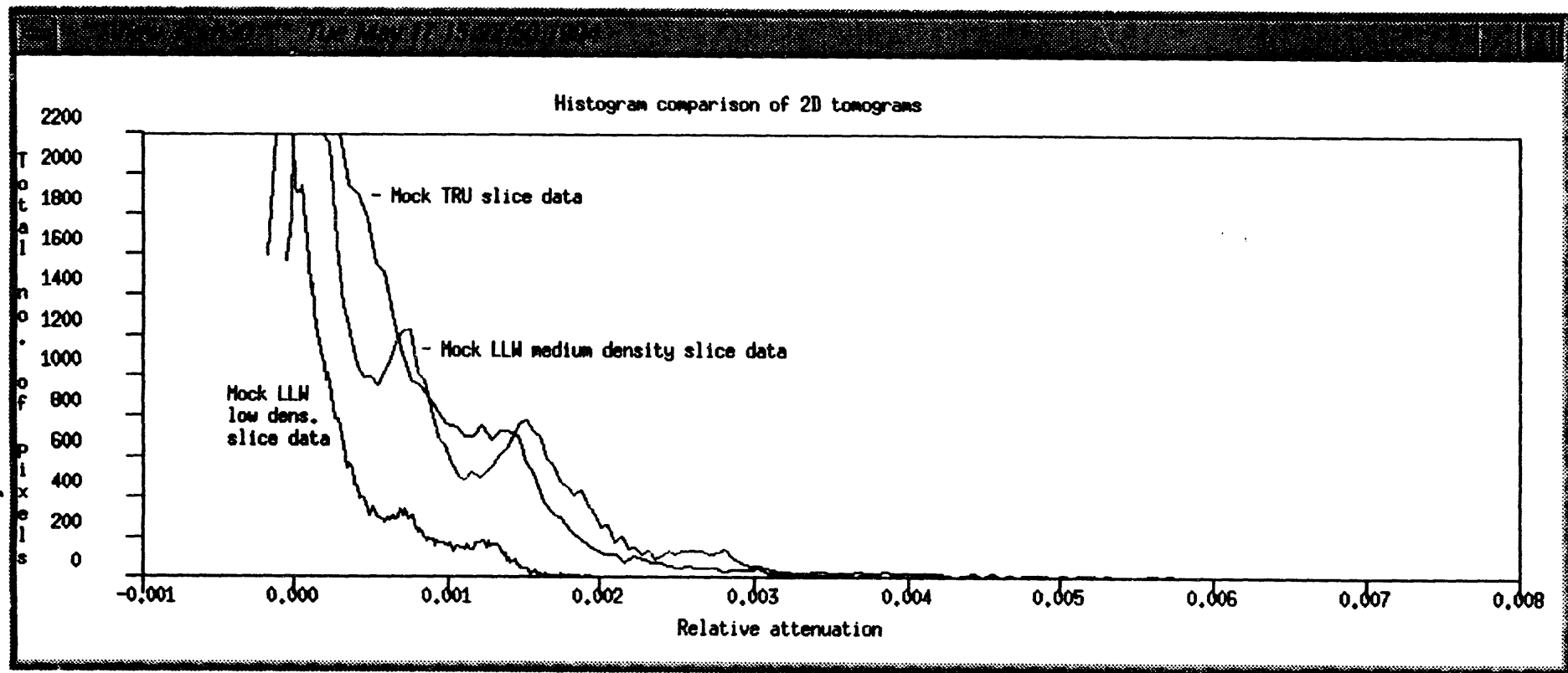


Figure 26: Histograms are plotted for the 2D CT images shown in Figure 16 as labeled.

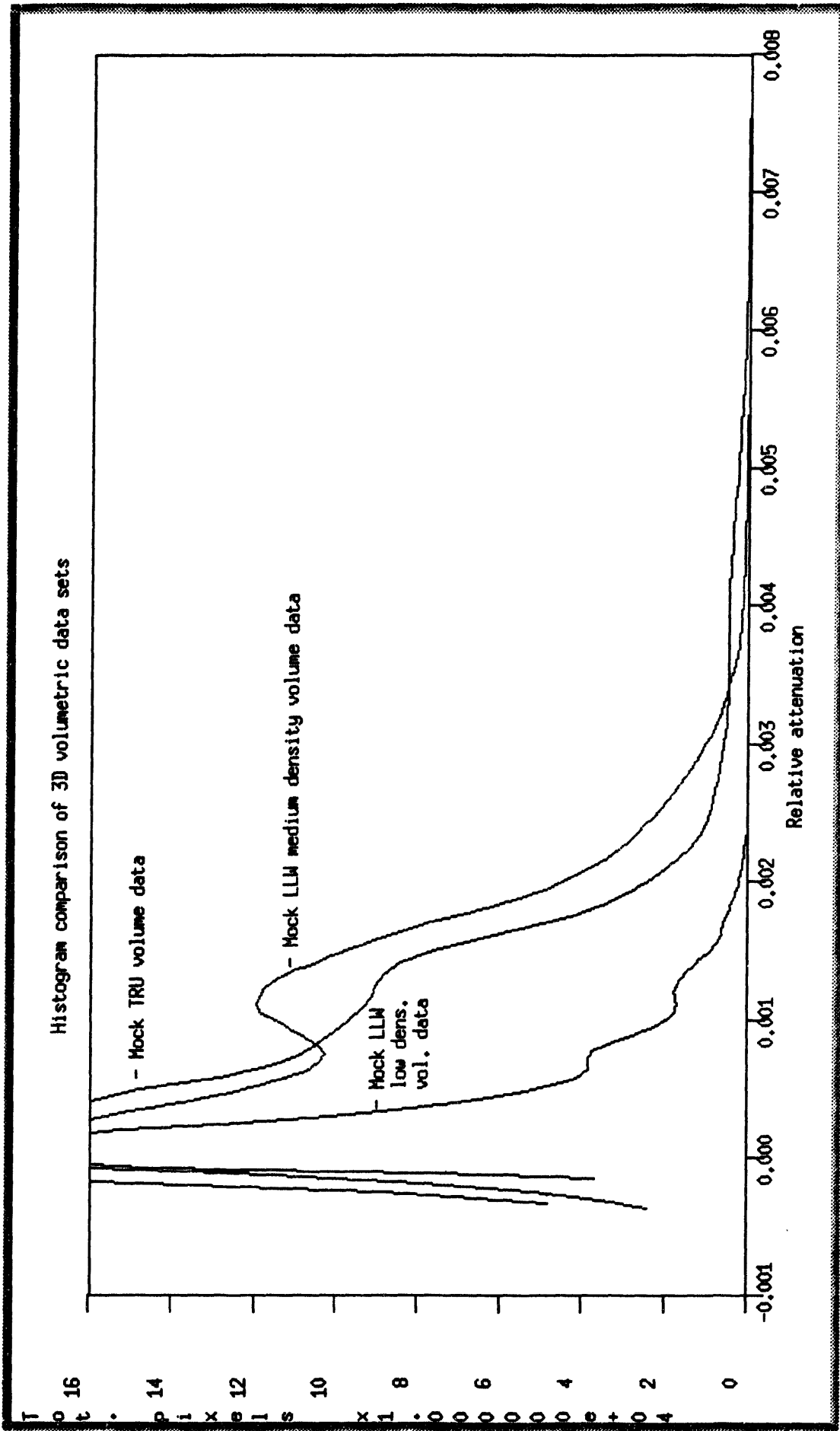


Figure 27: Histograms are plotted for a selected 75-slice volume data set for each mock-waste matrix as labeled.

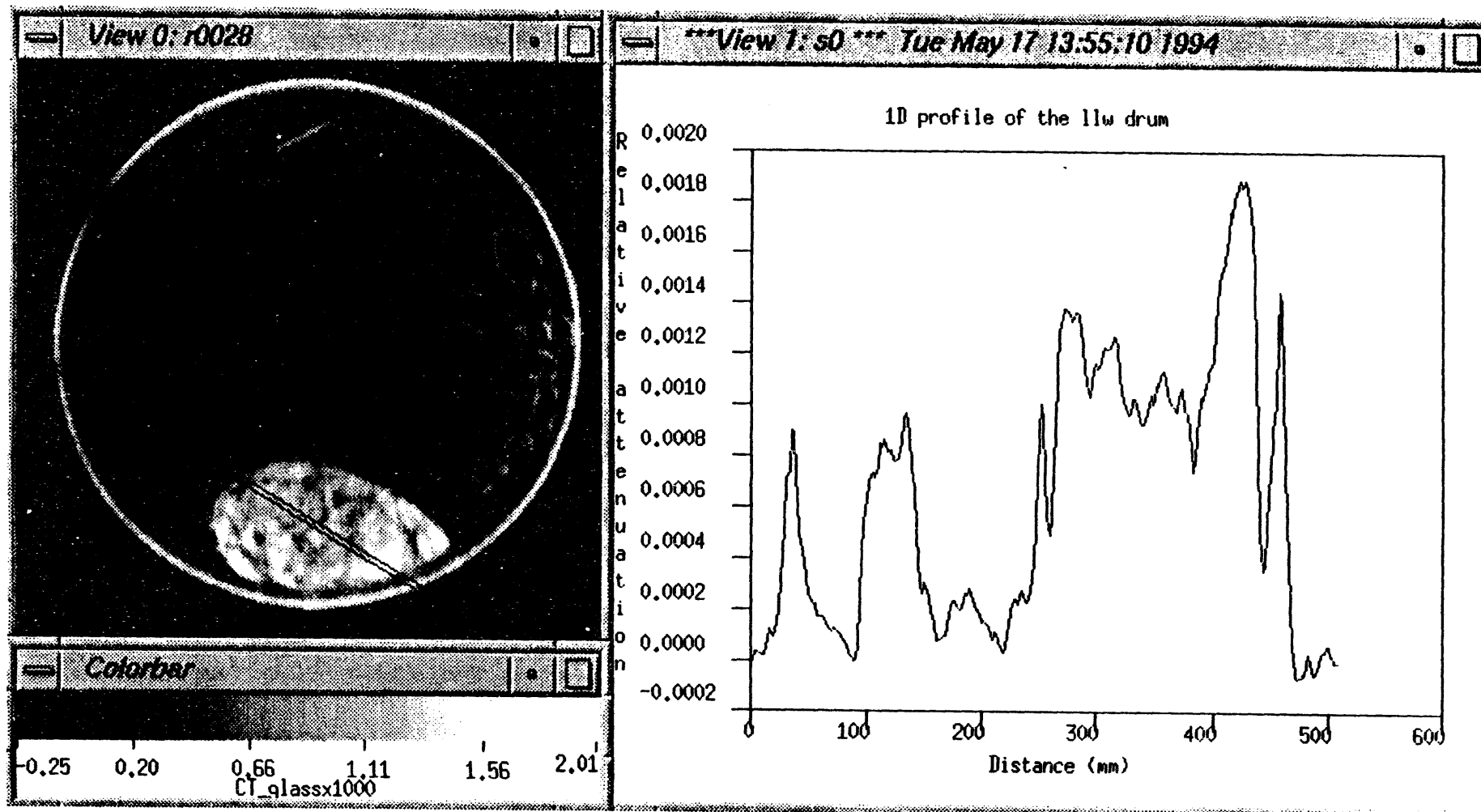


Figure 28: CT image for the real LLW drum with a glass matrix (left) and 1D profile plotted to the right as labeled.

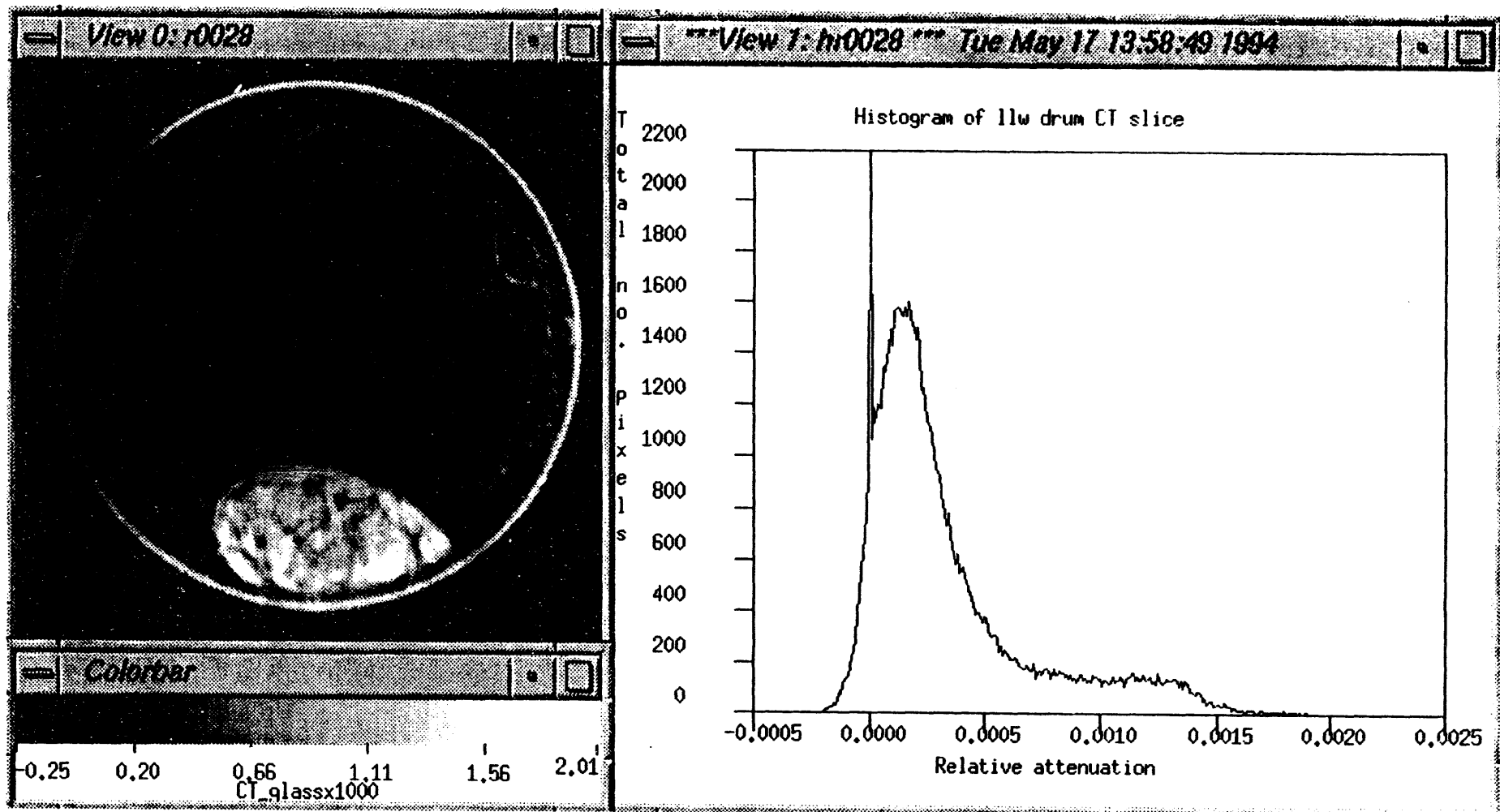


Figure 29: CT image and histogram for one cross-sectional area of the LLW drum with a glass-waste matrix.

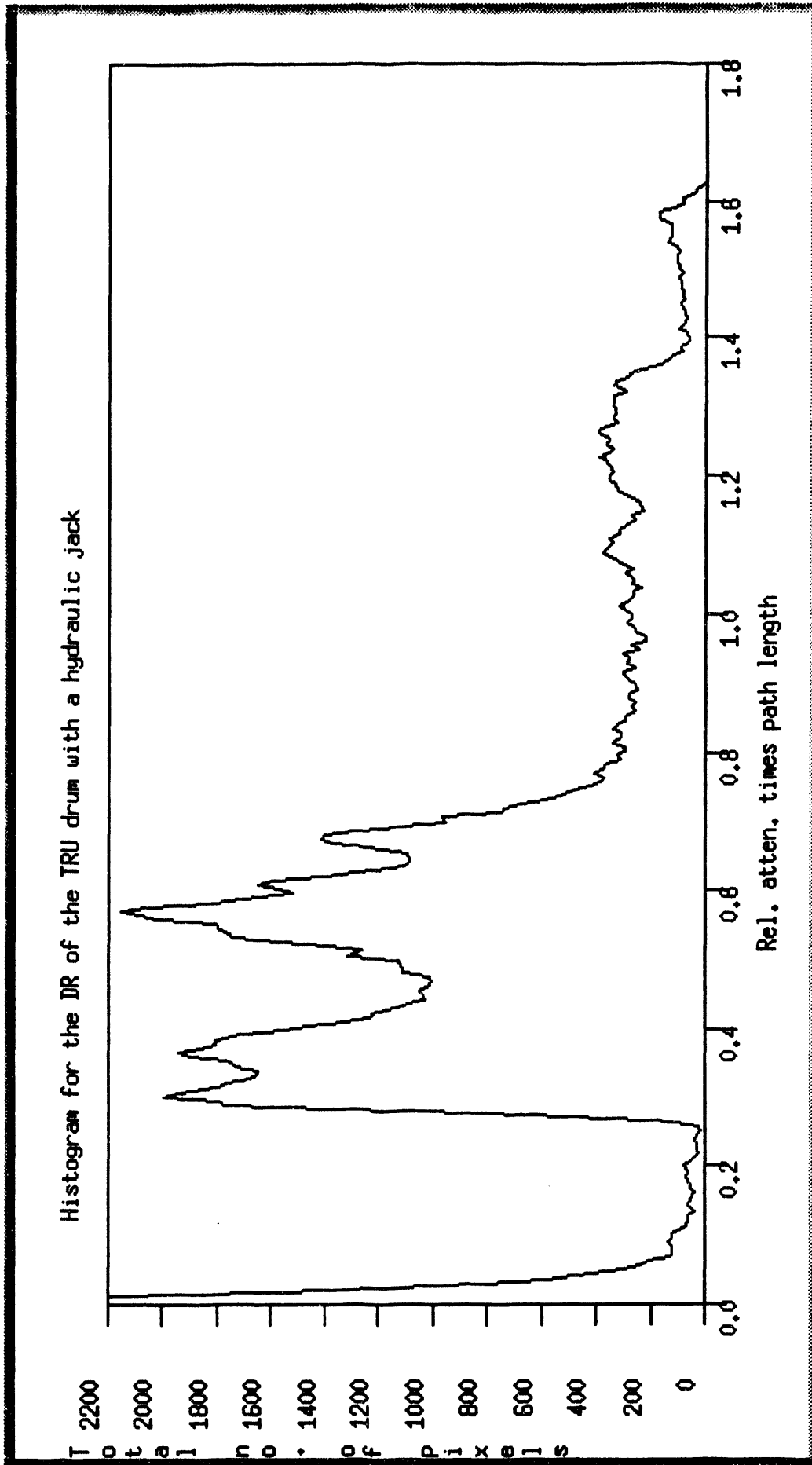


Figure 30: Histogram for the TRU waste drum DR image shown to the right in Figure 12.

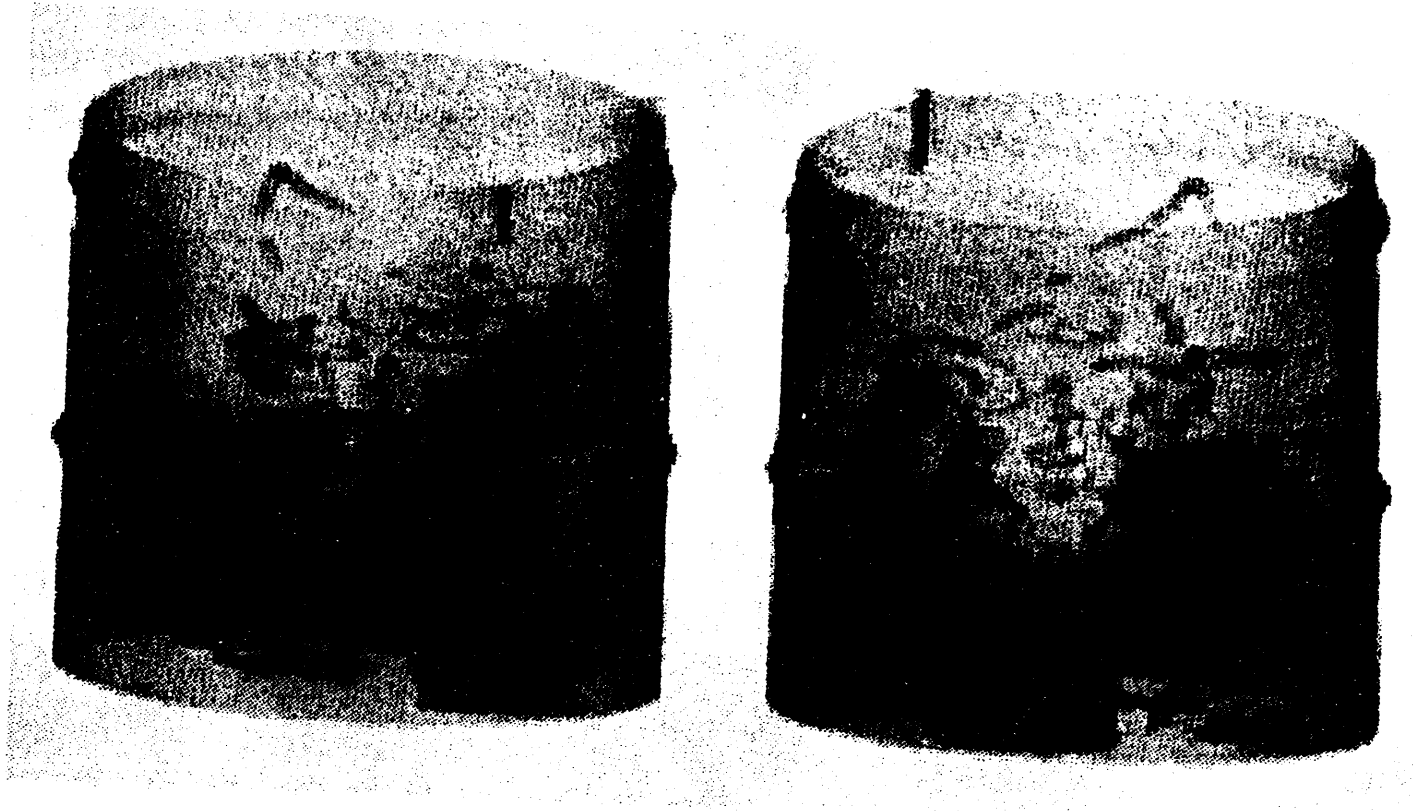


Figure 31: 3D volume rendered image of the TRU-waste drum that contains broken ceramic crucibles contaminated with Pu among other waste items.

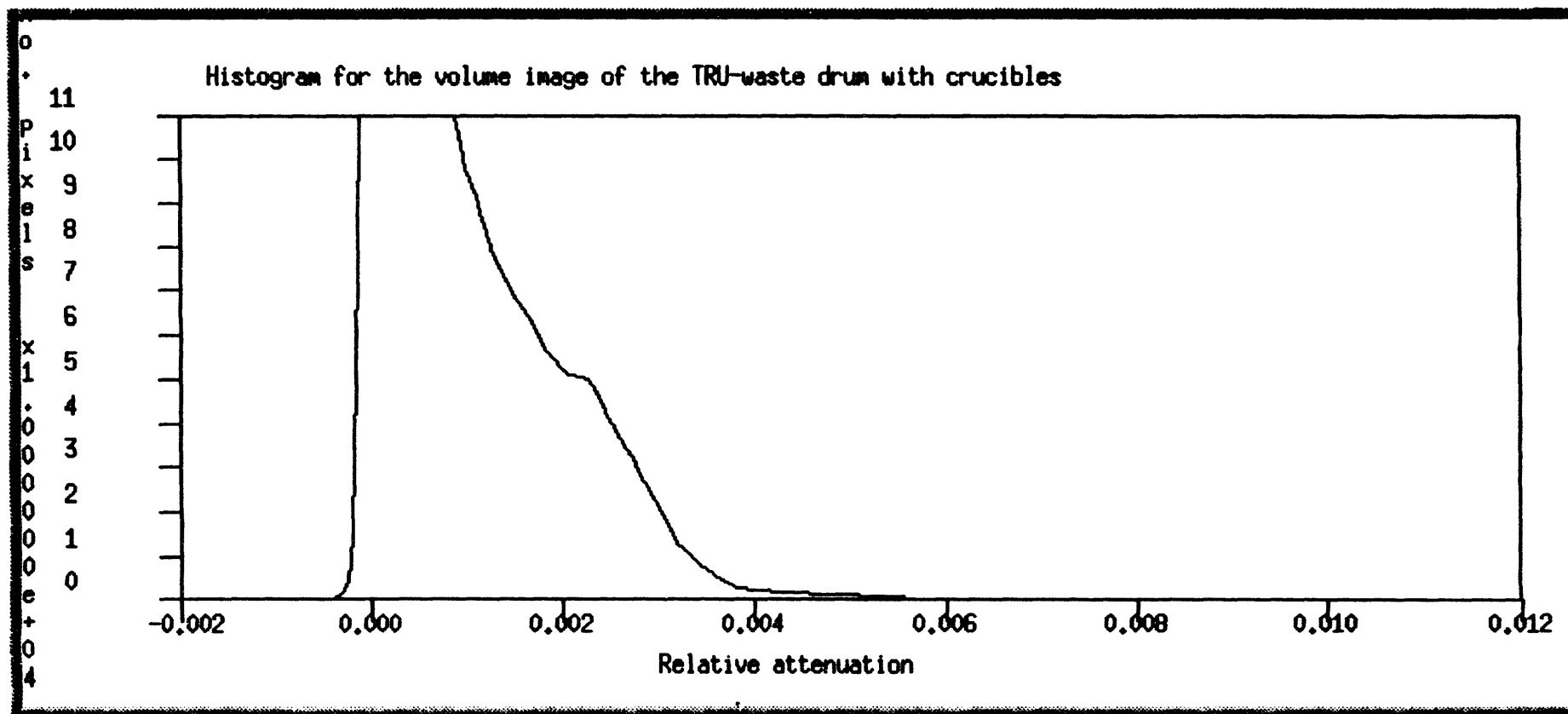


Figure 32: Histogram for the volume image of the TRU-waste drum represented in Figure 31.

**DATE
FILMED**

10/14/94

END

